Pressure dependent mechanical, optoelectronic and thermoelectric properties of K_2YAgBr_6 double perovskite: first principles study

Student ID: MS211307
Session: 2021-2022

Thesis submitted to the Department of Physics at
Jashore University of Science and Technology
in partial fulfillment of the requirements
for the degree of Masters of Science
in Physics

October 2024

Abstract

The development of lead-free halide double perovskites for renewable energy is an emerging field due to their interesting properties, such as high efficiency in light absorption, excellent stability under various environmental conditions, and potential for cost-effective large scale production. In this work, we computationally explored the mechanical, optoelectronic, and thermoelectric characteristics of halide double perovskite K_2YAgBr_6 using density functional theory up to 150 GPa applied pressure. Both the formation energy and tolerance factor ensure the structural stability of the compound. The presence of band edges at two different symmetry points indicates its indirect bandgap of 3.07 eV at ambient pressure, and the value of the band gap decreases with increasing pressure. The absorptivity and dielectric function values are increased with driving pressure. The absorption peak is shifted towards the lower energy region with increased hydrostatic pressure. The mechanical behaviors demonstrated that the material is mechanically stable and ductile, with its ductility further improved under pressure. By using the BoltzTraP code based on semi-classical Boltzmann transport theory, we estimate the thermoelectric properties of K_2YAgBr_6 under different hydrostatic pressure. The results show promising Seebeck coefficient and figure of merit, suggesting its potential for optoelectronics and thermoelectric applications.

Acknowledgements

Firstly, I praise and thank almighty Allah, the Lord of the worlds, the Most Merciful, the Guider of hearts, the Provider of sustenance, the Owner of life and death. I would like to thank my supervisor Dr. Mohammad Abdur Rashid, for his constant supervision, guidance and patience to complete my thesis properly. Also, my gratitude goes to all the faculty members of the Department of Physics for many helpful discussion at different times. I wish to extend my profound gratitude and appreciation to the Quantum Materials Simulation Lab (QMSL) for its resources throughout the course of my research. Working in the lab has been a very valuable and enlightening experience for me. The access to equipment and facilities within the lab has been instrumental in conducting experiments and collecting data, which provided the foundation for this research. I am deeply thankful to all the members of the research lab for their guidance, mentorship, and assistance. I am thankful to the different scientific journals and authors of many publications (listed as references) from which I got a lot of information and knowledge for my work. On a personal note, I would like to thank my parents for their sacrifice and support over the years. Their love and encouragement always give me mental support to continue my study smoothly.

Contents

Pressure dependent mechanical, optoelectronic and thermoelectric properties of K_2YAgBr_6 double perovskite: first principles study

1 Introduction **1**

2 Basic Quantum Mechanics **5**

2.1 Schrödinger equation 5

2.2 The wave function 6

2.3 Born-Oppenheimer (BO) approximation 8

2.4 The Hartree-Fock (HF) approach 9

2.5 Limitations of the Hartree-Fock (HF) approach 13

3 Density Functional Theory **16**

3.1 Overview 16

3.2 The electron density 17

3.3 Thomas-Fermi model 18

3.4 The Hohenberg-Kohn (HK) theorems 21

3.4.1 The HK theorem I 21

3.4.2 The HK theorem II 22

3.5 Kohn-Sham (KS) equation 23

3.5.1 Solving Khon-Shan equation 26

3.6 The exchange-correlation (XC) functional 27

3.7 Local Density Approximation (LDA) 28
3.8 Local Spin Density Approximation (LSDA) 29
3.9 Generalized Gradient Approximation (GGA) 34
3.10 LDA+U method 35

4 Results and Discussion **37**

4.1 Computational details 37
4.2 Structural properties 38
4.3 Electronic properties 40
4.4 Optical properties 45
4.4.1 Dielectric function 45
4.4.2 Absorption coefficient 48
4.4.3 Optical conductivity 49
4.4.4 Reflectivity 50
4.4.5 Refractive index 50
4.5 Thermoelectric properties 51
4.5.1 Electrical conductivity 52
4.5.2 Seebeck coefficient 53
4.5.3 Thermal conductivity 54
4.5.4 Power factor 55
4.5.5 Figure of merits 56
4.6 Mechanical properties 57

5 Conclusions **61**

Bibliography **62**

List of Figures

3.1 Flowchart of self-consistency loop for solving Kohn-Sham equation . . 27

4.1 Schematics representation of the crystal structure of K_2YAgBr_6. . . . 38

4.2 The calculated energy versus volume optimization curve of the K_2YAgBr_6 39

4.3 The calculated electronic band structure of K_2YAgBr_6 double perovskite under hydrostatic pressure up to 20 GPa. 41

4.4 The calculated electronic band structure of K_2YAgBr_6 double perovskite under hydrostatic pressure up to 150 GPa. 42

4.5 The total and partial density of states (PDOS) of b) K, c) Y, d) Ag and e) Br atoms in K_2YAgBr_6 at applied pressure. 43

4.6 Total density of states of K_2YAgBr_6 at different pressure. 44

4.7 The partial density of states (PDOS) of b) K, c) Y, d) Ag and e) Br atoms in K_2YAgBr_6 at applied pressure. 45

4.8 Calculated pressure-induced spectra of real portion of dielectric function of K_2YAgBr_6. 46

4.9 Calculated pressure-induced spectra of imaginary portion of dielectric function of K_2YAgBr_6. 47

4.10 Calculated pressure-induced spectra of absorption coefficient of K_2YAgBr_6. 48

4.11 Calculated pressure-induced spectra of optical conductivity of K_2YAgBr_6. 49

4.12 Calculated pressure-induced spectra of reflectivity of K_2YAgBr_6. . . . 50

4.13 Calculated pressure-induced spectra of refractive index of K_2YAgBr_6. 51

4.14 Calculated electrical conductivity under different hydrostatic pressure. 52

4.15 Calculated seebeck coefficient under different hydrostatic pressure. . 54

4.16 Calculated thermal conductivity under different hydrostatic pressure. 54

4.17 Calculated power factor under different hydrostatic pressure. 55

4.18 Calculated figure of merits under different hydrostatic pressure. . . . 56

List of Tables

4.1 Variation of lattice constants and band gaps of K_2YAgBr_6 under hydrostatic pressure up to 150 GPa 40

4.2 Calculated elastic constant C_{11}, C_{12}, C_{44}, Cauchy's pressure of K_2YAgBr_6 under hydrostatic pressure. 58

4.3 The calculated the Bulk modulus B (GPa), the Shear modulus G (GPa), Young's modulus Y (GPa), the elastic anisotropy factor (A), B/G ratio and Poisson's ratio (ν) of K_2YAgBr_6 under hydrostatic pressure. 59

Pressure dependent mechanical, optoelectronic and thermoelectric properties of K_2YAgBr_6 double perovskite: first principles study

Chapter 1

Introduction

The exponential increasing energy demand of human and continuously decreasing natural energy resousces has motivated the scientific community to look for smart and technologically advanced devices which can harvest energy from natural sources like the sun, wind and tides [1, 2]. Sun is one of the biggest sources of heat and light which could be converted into electrical energy using suitable optoelectronic and thermoelectric devices [3]. The efficiency of any such device depends upon the underlying material in these devices. In recent years, double perovskite materials have garnered significant attention due to their promising applications in various fields, including light-emitting diodes (LEDs), lasers, radiation detectors, and solar cells [4–8]. Among different types of double perovskites, a lot of work has been devoted to lead-based perovskite solar cells. For instance, $CH_3NH_3PbX_3$ (where X = I, Cl, Br) perovskites have been extensively explored [9–12]. Such kinds of solar cells are formed by mixing the inorganic materials in an organic matrix [13,14]. Their low processing cost, easy fabrication method, lightweight nature, suitable direct band gap, high absorption properties, and charge carriers effective masses are supposed to be the key features that make them suitable for optoelectronic devices [15–18]. However, their applications have long been limited by their unstable structure, high humidity sensitivity and the toxicity of lead [19].

Therefore, scientists are looking for lead-free materials that could curtile our dependence on fossil fuels and make eco-friendly devices [20]. With this consideration, halide-based double perovskites have attracted a lot of attention in recent years [21–23]. Double perovskite materials derived from a single perovskite compound represent by the formula ABX_3 [24]. The structural and compositional flexibility of single perovskites allows them to accommodate a variety of elements at A and B sites, which gives them wide spectrum of physical properties. This spectrum can further be extended using the substitution method where 50 % of A , B or both ions can be replaced with other elements [25]. Double perovskites are compounds whose unit cell doubles when half of the B-type element is replaced with another element B′ and denoted by the formula $A_2BB'X_6$ [26]. The presence of two different transition elements at the B site and an alkali or alkaline earth metal at the A site provides even greater flexibility and degrees of freedom, which bring double perovskites to the verge of new technological innovation. The possibility of a large variety of cationic substitutions reveals the potential of tuning the optoelectronic characteristics of this class of compounds [27, 28].

Recently, a lot of work is devoted to the optoelectronic and thermoelectric investigations of double perovskites because they provide an accommodative platform to incorporate a veriety of metal cation [29, 30]. For instance, Yang et al. They improved the stability and power conversion efficiency (PCE) of $Cs_2AgBiBr_6$ by slowing down crystal growth with thiourea during synthesis, achieving a PCE of 3.07 % and maintaining 95 % retention rate [31–33]. Yang et al. studied the interface engineering, band gap engineering and film quality optimization to improve the stability and conversion efficiency of perovskite solar cells [34]. In another report, Kangsabanik et al. performed an intuitive study and revealed how the double perovskite are overtaking simple perovskite due to their higher stability and better conversion efficiency [35]. Extensive studies exploring the multifunctional features of double perovskite oxides, hydroxides, nitrides, sulfides, and halides have been conducted. In addition, Wang et al. mixed graphene oxides with $Cs_2AgBiBr_6$ to examine their photo-catalytic degradation for hydrogen production [36, 37]. These compositions exposed higher stability for more than 120 hours.

The study of optoelectronic and thermoelectric properties reported by Ghulam M. Mustafa et al. [38] demonstrates that the non-toxic K_2YAgBr_6 double perovskite has ductility entity but the halide perovskite semiconductor shows large bandgap value 3.4 eV. It was observed that pressure effect on halide perovskites has seized great attention by the researchers in recent years [39–46], as it is generally known, effect of pressure has a vital role on the physical and chemical features of materials. The decrease of lattice volume of metal halides for the bulk phase is shown with enhanced pressure [41,44]. A material's different properties can be readily adjusted by applying a hydrostatic pressure [47–49]. For instance, pressure can modify the density of states close to the Fermi level, which can change electronic bandgaps or electrical conductivity [50]. In a theoretical study of cesium tin halides, it is exhibited that band gap decreases with decreasing lattice parameter [51]. Applying hydrostatic pressure can reduce the lattice parameter. The goal of our present work is to apply various hydrostatic pressures on K_2YAgBr_6 double perovskite in order to reduce the band gap and consequently it may improve the optical absorption as well as proficiency of solar cells, optoelectronic and other thermoelectric devices.

The present study deals with various hydrostatic pressure effects on the structural, electronic, optical, thermoelectric and mechanical properties of K_2YAgBr_6 double perovskite using density functional theory (DFT), utilizing the WIEN2k code [52]. Transport properties were calculated using the BoltzTraP code, where we computed thermal and electrical conductivities, the Seebeck coefficient and the power factor. This thesis is arranged in the following chapters: Chapter 1 includes some preliminary details about perovskites and cause of motivation for work on K_2YAgBr_6 double perovskite. Chapter 2 and 3 we discuss the basic quantum mechanics as the base of density functional theory. Starting from Schrödinger equation we dispute the criteria for the ground state wave function. We shortly discuss the Born oppenheimar approximation and the Hartree-Fock approach with its limitations in this chapter. We discuss the theoritical density functional theory. Starting with the Thomas Fermi model we discuss the Hohenberg Khon theorems, Kohn Sham equation with the equivalent flowchart and the exchange correletion functionals that can be used to solve a many body system . In chapter 4 describes the detail of com-

putetional method used for calculations. Chapter 5 present results of structural, electronic ,optical, thermoelectronic and mechanical properties followed by discussion on obtained results. In last chapter 6 conclusions was drawn to enlighten the future potential of this research.

Chapter 2

Basic Quantum Mechanics

2.1 Schrödinger equation

Schrödinger equation refers to a fundamental equation of quantum physics. The Schrödinger equation is a linear partial differential equation that governs the wave function of a quantum mechanical system. It is a key result in quantum mechanics, and its discovery was a significant landmark in the development of the subject. The equation is named after Erwin Schrödinger, who postulated the equation in 1925, and published it in 1926 [53]. The time-independent Schrödinger equation

$$\hat{H}\psi(\vec{r}) = E\psi(\vec{r}) \tag{2.1}$$

Where, $\hat{H}$ is the hamiltonian operator and ψ is the wave function. It is often impracticable to use a complete relativistic formulation of the formula; therefore Schrödinger himself postulated a non-relativistic approximation which is nowadays often used, especially in quantum chemistry.

Using the Hamiltonian for a single particle

$$\hat{H} = \hat{T} + \hat{V} = -\frac{\hbar^2}{2m}\vec{\nabla}^2 + V(\vec{r}) \tag{2.2}$$

leads to the (non-relativistic) time-independent single-particle Schrödinger equation

$$E\psi(\vec{r}) = \Big[-\frac{\hbar^2}{2m}\vec{\nabla}^2 + V(\vec{r})\Big]\psi(\vec{r}). \tag{2.3}$$

For N particles in three dimensions, the Hamiltonian is

$$\hat{H} = \sum_{i=1}^{N} \frac{\hat{p}_i^2}{2m_i} + V(\vec{r}_1, \vec{r}_2, ...\vec{r}_N) = -\frac{\hbar^2}{2}\sum_{i=1}^{N}\frac{1}{m_i} + V(\vec{r}_1, \vec{r}_2, ...\vec{r}_N) \tag{2.4}$$

The corresponding Schrödinger equation reads

$$E\psi(\vec{r}_1, \vec{r}_2, ...\vec{r}_N) = \Big[-\frac{\hbar^2}{2}\sum_{i=1}^{N}\frac{1}{m_i}\nabla_i^2 + V(\vec{r}_1, \vec{r}_2, ...\vec{r}_N)\Big]\psi(\vec{r}_1, \vec{r}_2, ...\vec{r}_N) \tag{2.5}$$

Special cases are the solutions of the time-independent Schrödinger equation, where the Hamiltonian itself has no time-dependency (which implies a time-independent potential $V(\vec{r}_1, \vec{r}_2, ...\vec{r}_N)$ and the solutions therefore describe standing waves which are called stationary states or orbitals). Furthermore, the left hand side of the equation reduces to the energy eigenvalue of the Hamiltonian multiplied by the wave function, leading to the general eigenvalue equation

$$E\psi(\vec{r}_1, \vec{r}_2, ...\vec{r}_N) = \hat{H}\psi(\vec{r}_1, \vec{r}_2, ...\vec{r}_N) \tag{2.6}$$

Again, using the many-body Hamiltonian, the Schrödinger equation becomes

$$E\psi(\vec{r}_1, \vec{r}_2, ...\vec{r}_N) = \Big[-\frac{\hbar^2}{2}\sum_{i=1}^{N}\frac{1}{m_i}\nabla_i^2 + V(\vec{r}_1, \vec{r}_2, ...\vec{r}_N)\Big]\psi(\vec{r}_1, \vec{r}_2, ..., \vec{r}_N) \tag{2.7}$$

2.2 The wave function

A wave function is a mathematical representation of a particle's quantum state as a function of momentum, position, time and spin in quantum physics. It contains all the information about the particle's state. A wave function is represented by the Greek letter ψ. The probability of finding an electron within the matter-wave

may be explained using a wave function. This may be produced by incorporating an imaginary number that is squared to give a real number solution resulting in an electrons position. Max Born developed a probabilistic interpretation of the wave function as a probability density, which is a major principle of the Copenhagen interpretation of quantum mechanics [54, 55].

$$|\psi(\vec{r}_1, \vec{r}_2, ...\vec{r}_N)|^2 d\vec{r}_1, d\vec{r}_2, ...\vec{r}_N. \tag{2.8}$$

The particles $1, 2, ..., N$ are all present at the same time in the corresponding volume element $d\vec{r}_1, d\vec{r}_2, ...d\vec{r}_N$ which is the probability that is specified by equation (2.8) [56]. If the positions of two particles are exchanged, the total probability density cannot be affected. That is to written as,

$$|\psi(\vec{r}_1, \vec{r}_2, ...\vec{r}_i, \vec{r}_j, ...\vec{r}_N)|^2 = |\psi(\vec{r}_1, \vec{r}_2, ...\vec{r}_j, \vec{r}_i, ...\vec{r}_N)|^2. \tag{2.9}$$

The symmetrical and anti-symmetrical wave functions are two possible wavefunction behaviours during a particle exchange. The symmetrical wave function remains unchanged as a result of such exchange, which corresponds to bosons (integer or zero spin). However, the anti-symmetrical wave function shifts it's sign to correspond to fermions (half-integer spin) [57,58]. Because electrons are fermions, in this text may explore the anti-symmetric fermion wave function. The Pauli exclusion principle, which states that no two electrons may occupy the same orbital, is followed by the anti-symmetric fermion wave function. Another result of probability interpretation is the normalization of the wave function [57]. A particle's wave function must be normalized. The probability of finding the particle somewhere in space is unity as

$$\int d\vec{r}_1 \int d\vec{r}_2 ... \int d\vec{r}_N |\psi(\vec{r}_1, \vec{r}_2, ...\vec{r}_N|^2 = 1. \tag{2.10}$$

Equation (2.10) is physically valid. Continuous and square-integrable wave functions are required. In quantum physics, any wave function that is not continuous and square-integrable has no physical meaning [59]. When we calculate the expectation values of operators with a wave function, we get the expectation value of the

corresponding observable for that wavefunction, which is another important aspect of the wave function. This may be expressed for an observable $O(\vec{r}_1, \vec{r}_2, ...\vec{r}_N)$ as

$$O = \langle O \rangle = \int d\vec{r}_1 \int d\vec{r}_2 \int d\vec{r}_N \psi^*(\vec{r}_1, \vec{r}_2, ...\vec{r}_N)\hat{O}\psi(\vec{r}_1, \vec{r}_2, ...\vec{r}_N). \tag{2.11}$$

2.3 Born-Oppenheimer (BO) approximation

The Schrödinger equation of a many-body system is,

$$\hat{H}_{tot}\psi(\{\vec{R}_I\}, \{\vec{r}_i\}) = E\psi(\{\vec{R}_I\}, \{\vec{r}_i\}). \tag{2.12}$$

Where, H_{tot} is the total Hamiltonian, E is the total energy and $\psi(\{\vec{R}_I\}, \{\vec{r}_i\})$ is the total wave function of the system. The total Hamiltonian of a many-body system consisting of nuclei and electrons can be written as

$$\begin{aligned}\hat{H}_{tot} = -\sum_I \frac{\hbar^2}{2M_I}\vec{\nabla}^2_{\vec{R}_I} - \sum_i \frac{\hbar^2}{2m_e}\vec{\nabla}^2_{\vec{r}_i} + \frac{1}{2}\sum_{I,J}\frac{Z_I Z_J e^2}{|\vec{R}_I - \vec{R}_J|} \\ + \frac{1}{2}\sum_{i,j}\frac{e^2}{|\vec{r}_i - \vec{r}_j|} - \sum_{I,i}\frac{Z_I e^2}{|\vec{R}_I - \vec{r}_i|},\end{aligned} \tag{2.13}$$

where, the indexes I,J run on nuclei, i and j on electrons, $\vec{R}_I$ and M_I are position and mass of the nuclei, $\vec{r}_i$ and m_e are position and mass of the electrons. The first term of the above equation represents the kinetic energy of the Nuclei. Second term represents the kinetic energy of the electrons. Third term $\frac{1}{2}\sum_{I,J}\frac{Z_I Z_J e^2}{|\vec{R}_I - \vec{R}_J|}$ is for potential energy of nucleus-nucleus Coulomb interaction, the fourth term is the potential energy electron-electron Coulomb interaction and the last term is the potential energy of nucleus-electron Coulomb interaction.

As nuclei are significantly heavier than electrons (the mass of a proton is about 1836 times the mass of an electron), the electrons travel considerably more quickly than the nuclei [59]. In that case, Born-Oppenheimer (BO) approximation was proposed by Born and Oppenheimer in 1927. The Born-Oppenheimer approximation is an assumption that it is possible to distinguish equation(2.12) between the nuclear and

electronic motions of molecules. Consider the nuclei to be static, classical potential with respect to the electron, then address the electronic issue without further consideration of the nuclei [60] . On the timeline of the electronic transition, it is possible to claim that the core movement can be disregarded, i.e., it has no bearing on them [61–63]. Adopting Born-Oppenheimer approximation the electronic hamiltonian the becomes

$$\hat{H} = -\sum_i \frac{\hbar^2}{2m_e}\vec{\nabla}^2_{\vec{r}_i} + \frac{1}{2}\sum_{i,j}\frac{e^2}{|\vec{r}_i - \vec{r}_j|} - \sum_{I,i}\frac{Z_I e^2}{|\vec{R}_I - \vec{r}_i|}. \tag{2.14}$$

The BO approximation's importance lies in it's ability to distinguish between the motion of electrons and nuclei. The starting point of DFT is the electron motion in a static external potential $V_{ext}(\vec{r})$ created by the nucleus. Born and Huang expanded the BO approximation, giving it the name Born-Huang (BH) approximation, to account for more non-adiabatic effects in the electronic Hamiltonian than the BO approximation did.

2.4 The Hartree-Fock (HF) approach

In order to find a suitable strategy to approximate the analytically not accessible solutions of many-body problems, a very useful tool is variational calculus, similar to the least action principle of classical mechanics. By the use of variational calculus, the ground state wave function ψ_0 , which corresponds to the lowest energy of the system E_0 can be approached. Hence, for now only the electronic Schrödinger equation is of interest, therefore in the following sections we set $\hat{H} \equiv \hat{H}_{el}$, $E \equiv E_{el}$, and so on. Observables in quantum mechanics are calculated as the expectation values of operators [64, 65]. The energy as observable corresponds to the Hamilton operator, therefore the energy corresponding to a general Hamiltonian can be calculated as

$$E = \langle \hat{H} \rangle = \int d\vec{r}_1 \int d\vec{r}_2 ... \int d\vec{r}_N \psi*(\vec{r}_1, \vec{r}_2, ..., \vec{r}_N)\hat{H}\psi(\vec{r}_1, \vec{r}_2, ..., \vec{r}_N) \tag{2.15}$$

The Hatree-Fock techique is based on the principle that the energy obtained by any (normalized) trial wave function other than the actual ground state wave function is always an upper bound, i.e. higher than the actual ground state energy. If the trial function happens to be the desired ground state wave function, the energies are equal

$$E_{trial} \geq E_0 \tag{2.16}$$

$$E_{trial} = \int d\vec{r}_1 \int d\vec{r}_2 ... \int d\vec{r}_N \psi^*_{trial}(\vec{r}_1, \vec{r}_2, ..., \vec{r}_N) \hat{H} \psi_{trial}(\vec{r}_1, \vec{r}_2, ..., \vec{r}_N) \tag{2.17}$$

and

$$E_0 = \int d\vec{r}_1 \int d\vec{r}_2 ... \int d\vec{r}_N \psi^*_0(\vec{r}_1, \vec{r}_2, ..., \vec{r}_N) \hat{H} \psi_0(\vec{r}_1, \vec{r}_2, ..., \vec{r}_N) \tag{2.18}$$

For a detailed description of this notation, the reader is referred to the original publication [66]. In that notation, equation (2.15) to (2.17) are expressed as

$$\langle \psi_{trial} | \hat{H} | \psi_{trial} \rangle = E_{trial} \geq E_0 = \langle \psi_0 | \hat{H} | \psi_0 \rangle \tag{2.19}$$

Proof: The eigenfunctions ψ_i of the Hamiltonian $\hat{H}$ (each corresponding to an energy eigenvalue E_i form a complete basis set, therefore any normalized tria wave function ψ_{trial}can be expressed as linear combination of those eigenfunctions [65].

$$\psi_{trial} = \sum_i \lambda_i \psi_i \tag{2.20}$$

The assumption is made that the eigenfunctions are orthogonal and normalized. Hence it is requested that the trial wave function is normalized, it follows that

$$\langle \psi_{trial} | \psi_{trial} \rangle = 1 = \langle \sum_i \lambda_i \psi_i | \sum_j \lambda_j \psi_j \rangle = \sum_i \sum_j \lambda^*_i \lambda_j \langle \psi_i | \psi_j \rangle = \sum_j |\lambda_j|^2 \tag{2.21}$$

On the other hand, following (2.19) and (2.21)

$$E_{trial} = \langle\psi_{trial}|\hat{H}|\psi_{trial}\rangle = \langle\sum_i \lambda_i\psi_i|\hat{H}|\sum_j \lambda_j\psi_j\rangle = \sum_j E_j|\lambda_j|^2 \tag{2.22}$$

Together with the fact that the ground state energy E_0 is per definition the lowest possible energy, and therefore has the smallest eigenvalue ($E_0 \leq E_i$), it is found that

$$E_{trial} = \sum_j E_j|\lambda_j|^2 \geq E_0 \sum_j |\lambda_j|^2 \tag{2.23}$$

what resembles equation (2.26). Equations(2.22) to (2.30) also include that a search for the minimal energy value while applied on all allowed N-electron wave-functions will always provide the ground-state wave function (or wave functions, in case of a degenerate ground state where more than one wave function provides the minimum energy). Expressed in terms of functional calculus,where $\psi \rightarrow N$ addresses all allowed N-electron wave functions,

$$E_0 = \min_{\psi\rightarrow N} E[\psi] = \min_{\psi\rightarrow N}\langle\psi|\hat{H}|\psi\rangle = \min_{\psi\rightarrow N}\langle\psi|\hat{T}+\hat{V}+\hat{U}|\psi\rangle \tag{2.24}$$

Due to the vast number of alternative wave functions on the one hand and processing power and time constraints on the other, this search is essentially unfeasible for N-electron systems. Restriction of the search to a smaller subset of potential wave functions, as in the Hartree-Fock approximation, is conceivable. A slater determinant is a formula in quantum mechanics that desceibes the wave function of a multi-fermionic system. It satisfies anti-symmetric criteria, and thus the Pauli's principle, by changing sign when two electrons are exchanged (or other fermions). Only a small fraction of all potential fermionic wave functions can be expressed as a single slater determinant, but because of their simplicity, they are an important and useful subset. In the Hartree- Fock approach, the search is restricted to approximations of the N-electron wave function by an antisymmetric product of N (normalized) one electron wave functions, the so called spin- orbitals $\chi_i(\vec{x}_i)$ [67]. A

wave function of this type is called Slater-determinant, and reads.

$$\psi_0 \approx \phi_{SD} = (N!)^{-\frac{1}{2}} \begin{vmatrix} \chi_1(\vec{x}_1) & \chi_2(\vec{x}_1) & \cdots & \chi_N(\vec{x}_1) \\ \chi_1(\vec{x}_2) & \chi_2(\vec{x}_2) & \cdots & \chi_N(\vec{x}_2) \\ \vdots & \vdots & \ddots & \vdots \\ \chi_1(\vec{x}_N) & \chi_2(\vec{x}_N) & \cdots & \chi_N(\vec{x}_N) \end{vmatrix} \tag{2.25}$$

It is important to notice that the spin-orbitals $\chi_i(\vec{x}_i)$ are not only depending on spatial coordinates but also on a spin coordinate which is introduced by a spin function, $\vec{x}_i = \vec{r}_i, s$. Returning to the variational principle and equation (2.25), the ground state energy approximated by a single slater determinant becomes.

$$E_0 = \min_{\phi_{SD} \to N} E[\phi_{SD}] = \min_{\phi_{SD} \to N} \langle \phi_{SD} | \hat{H} | \phi_{SD} \rangle = \min_{\phi_{SD} \to N} \langle \phi_{SD} | \hat{T} + \hat{V} + \hat{U} | \phi_{SD} \rangle \tag{2.26}$$

A general expression for the Hartree-Fock Energy is obtained by usage of the Slater determinant as a trial function.

$$E_{HF} = \langle \phi_{SD} | \hat{H} | \phi_{SD} \rangle = \langle \phi_{SD} | \hat{T} + \hat{V} + \hat{U} | \phi_{SD} \rangle \tag{2.27}$$

For the sake of brevity, a detailed derivation of the final expression for the Hartree-Fock energy is omitted. It is a straightforward calculation found for example in the Book by Schwabl [64]. The final expression for the Hartree-Fock energy contains three major parts: [67].

$$E_{HF} = \langle \phi_{SD} | \hat{H} | \phi_{SD} \rangle = \sum_{i}^{N} (i|\hat{h}|i) + \frac{1}{2} \sum_{i}^{N} \sum_{j}^{N} [(ii|jj) - (ij|ji)] \tag{2.28}$$

with

$$(i|\hat{h_i}|i) = \int \chi_i^*(\vec{x}_i)[-\frac{1}{2}\vec{\nabla}_i^2 - \sum_{k=1}^{M} \frac{Z_k}{r_{ik}}]\chi_i(\vec{x}_i) d\vec{x}_i, \tag{2.29}$$

$$(ii|jj) = \iint |\chi_i(\vec{x}_i)|^2 \frac{1}{r_{ij}} |\chi_j(\vec{x}_j)|^2 d\vec{x}_i d\vec{x}_j, \tag{2.30}$$

$$(ij|ji) = \iint \chi_i(\vec{x}_i)\chi_j^*(\vec{x}_j)\frac{1}{r_{ij}}\chi_j(\vec{x}_j)\chi_i^*(\vec{x}_i)d\vec{x}_i d\vec{x}_j \tag{2.31}$$

The first term corresponds to the kinetic energy and the nucleus-electron interactions, $\hat{h}$ denoting the single particle contribution of the Hamiltonian, whereas the latter two terms correspond to electron-electron interactions. They are called Coulomb and exchange integral, respectively. Examination of equations (2.30) to (2.31) furthermore reveals, that the Hartree-Fock energy can be expressed as a functional of the spin orbitals $E_{HF} = E[\{\chi_i\}]$. Thus,variation of the spin orbitals leads to the minimum energy. An important point is that the spin orbitals remain orthonormal during minimization.This restriction is accomplished by the introduction of Lagrangian multipliers λ_i in the resulting equations, which represent the Hartree-Fock equations.

$$\hat{f}\chi_i = \lambda_i\chi_i \qquad i = 1, 2, ..., N \tag{2.32}$$

with

$$\hat{f}_i = -\frac{1}{2}\vec{\nabla}_i^2 - \sum_{k=1}^{M}\frac{Z_k}{r_{ik}} + \sum_{i}^{N}[\hat{J}_j(\vec{x}_i) - \hat{K}_j(\vec{x}_i)] = \hat{h}_i + \hat{V}^{HF}(i) \tag{2.33}$$

Finally one arrives at the Fock operator for the i-th electron. In similarity to(2.28) to (2.31), the first two terms represent the kinetic and potential energy due to nucleus-electron interaction, collected in the core Hamiltonian $\hat{h}_i$, whereas the latter terms are sums over the Coulomb operators $\hat{J}_j$ and the exchange operators $\hat{K}_j$ with the other j electrons, which form the Hartree-Fock potential $\hat{V}$. There are major approximation of Hartree-Fock can be seen. The two electron repulsion operator from the original Hamiltonian is exchanged by a one-electron operator $\hat{V}$ which describes the repulsion in average.

2.5 Limitations of the Hartree-Fock (HF) approach

Atoms as well as molecules can have an even or odd number of electrons. If the number of electrons is even and all of them are located in double occupied spatial

orbitals ϕ_i, the compound is in a singlet state. Such systems are called closed-shell systems. Compounds with an odd number of electrons as well as compounds with single occupied orbitals, i.e. species with triplet or higher ground state, are called open-shell systems respectively. These two types of systems correspond to two different approaches of the Hartree-Fock method. In the restricted HF method (RHF), all electrons are considered to be paired in orbitals whereas in the unrestricted HF (UHF)-method this limitation is lifted totally. It is also possible to describe open-shell systems with a RHF approach where only the single occupied orbitals are excluded which is then called a restricted open-shell HF (ROHF) which is an approach closer to reality but also more complex and therefore less popular than UHF [67].

There are also closed-shell systems which require the unrestricted approach in order to get proper results. For instance, the description of the dissociation of H_2 (i.e. the behavior at large internuclear distance), where one electron must be located at one hydrogen atom, can logically not be obtained by the use of a system which places both electrons in the same spatial orbital. Therefore the choice of method is always a very important point in HF calculations [68].Kohn states several $M = p^5$ with $3 \leq p \leq 10$ parameters for an output with adequate accuracy in the investigations of the H_2 system [69]. For a system with $N = 100$ electrons, the number of parameters rises to,

$$M = p^{3N} = 3^{300} to 10^{300} \approx 10^{150} to 10^{300} \tag{2.34}$$

According to the equation (2.34), energy reduction would have to be done in a space with at least 10^{150} dimension, which is well above current computer capabilities. As a result, HF methods are limited to situations involving a modest number of electron ($N \approx 10$), This barrier commonly referred to as the exponential wall because of the exponential component in equation (2.34) [69]. Since a many electron wave function cannot be described entirely by a single Slater determinant, the energy obtained by HF calculations is always larger than the exact ground state energy. The most accurate energy obtainable by HF-methods is called the Hartree-Fock-limit. The

Hartree-Fock-limit is the most precise energy that can be calculated using HF-methods. Since a many electron wave function cannot be described entirely by a single Slater determinant, the energy obtained by HF calculations is always larger than the exact ground state energy. The most accurate energy obtainable by HF-methods is called the Hartree-Fock limit. The difference between E_{HF} and E_{exact} is called correlation energy and can be denoted as,

$$E_{corr}^{HF} = E_{min} - E_{HF}. \tag{2.35}$$

Despite the fact that E_{corr} is usually small against E_{min}, as in the example of a N_2 molecule where

$$E_{corr}^{HF} = 14.9eV < 0.001.E_{min}, \tag{2.36}$$

For instance, the experimental dissociation energy of the N_2 molecule is

$$E_{diss} = 9.9eV < E_{corr}, \tag{2.37}$$

which corresponds to a large contribution of the correlation energy to relative energies such as reaction energies which are of particular interest in quantum chemistry. The main contribution to the correlation energy arises from the mean field approximation used in the HF-method. That means one electron moves in the average field of the other ones, an approach which completely neglects the intrinsic correlation of the electron movements. To get a better understanding what that means, one may picture the repulsion of electrons at small distances which clearly cannot be covered by a mean-field approach like the Hartree-Fock method.

Chapter 3

Density Functional Theory

3.1 Overview

Computational methods have now become an essential aspect of the scientific world, particularly in the calculation of issues. Computers and numerical approaches are important for issues involving enormous quantities of particles,data and so on that cannot be solved analytically. Additionally, it requires a large amount of funding or resources for the experiment. DFT is a type of ab initio method that is often referred to as a computational quantum mechanical modeling method. The method is well-known at the matter of quantum chemistry, condensed matter physics, materials science et cetera. The application of this method starts with remedying the many body Schrödinger equation equation problem. However, DFT is more than just another method to solve the Schrödinger equation equation. DFT provides an entirely distinct approach to any interacting problem, translating it perfectly to more simple non-interacting problem. This methodology is broadly utilized for resolving a variety of issues, with the electronic structure problem being the most common [70]. In DFT, the electron density is used as the fundamental factor, instead of the wave-function. Another method for solving the many-body Schrödinger equation equation is the Hartree-Fock approach, that use wave-functions to describe the elec-

tronic figure of atoms and substance. However, this methods has several drawbacks, including a high cost of calculation time for investigating big systems. But DFT has demonstrated superior accuracy at a reduced computing cost, making it superior to all other approaches. This facts makes DFT the most useful method to analyze electronic structure. Walter Kohn with his co-workers developed this "Density functional theory" and find out the way of using the electron density to resolve the Schrödinger equation equation. For his timeworn work, he got novel prize in 1998 [69]. The chapter describes their work in broad strokes, beginning with fundamental quantum physics, its issues, and how DFT resolves them.

3.2 The electron density

The electron density (for N electrons) as the basic variable of density fuctional theory is defined as [71] In electronic system, the number of electron per unit volume in a given state is the electron density for a state designated by $n(\vec{r})$. Its formula in terms of ψ is

$$n(\vec{r}) = N \sum_{s_1} \int d\vec{x}_2 ... \int d\vec{x}_N \psi^*(\vec{x}_1, \vec{x}_2, ...\vec{x}_N)\psi(\vec{x}_1, \vec{x}_2, ..., \vec{x}_N). \tag{3.1}$$

The electron density can also be described as a measurably obserable quantity based simply on spatial coordinates if the spin coordinates are further neglected [69]

$$n(\vec{r}) = N \int d\vec{r}_2 ... \int d\vec{r}_N \psi^*(\vec{r}_1, \vec{r}_2, ..., \vec{r}_N)\psi(\vec{r}_1, \vec{r}_2, ..., \vec{r}_N) \tag{3.2}$$

with, for instance, an X-ray diffraction measurement. It must be confirmed that a method employing the electron density as a variable actually contains all necessary information about the system before it is presented. That entails, specifically, that it must include details on the electron number n as well as the external potential denoted by $\hat{V}$. By integrating the electron density over the spatial variables, one may get the total number of electrons.

$$N = \int d\vec{r} n(\vec{r}). \tag{3.3}$$

For an atom in its ground state the density decreases monotonically away from the nucleus [72]. The electron density at any atomic nucleus in an atom, molecule, or solid has a finite value. Hohenberg and Kohn pointed out that if one knows the density of the ground state of a many electron system, one can deduce from it the external potential in which the electrons reside, up to an overall constant [60]. It must be kept in mind that the only ways in which two many electron problem can differ are in the external potentials $\hat{V}$ and in the number of electrons that reside in the potentials. According to this results, both of these external parameters are determined by the electron density, so one can say that the density completely determines the many body problem. This statement is surprising, because the density is a real function of a single spatial variable while complete quantum mechanical wave function needs N variables for its description. The starting point of the theory is the observation of Hohenberg and Kohn that electron density contains in principle all the information contained in a many electron wave function.

3.3 Thomas-Fermi model

The assumptions stated by Thomas are that, electrons are distributed uniformly in a six dimentional phase space for the motion of an electron at the rate of two for each h^3 of volume and that there is an effective potential field that is itself determined by the nuclear charge and this distribution of electrons. The Thomas Fermi formula for electron density can be derived from these assumptions [60]. Let us consider the space devided into many small cubes, each of side l and volume $\delta V = l^3$, each containing some fixed number of electrons δN and we assume that the electrons in each shell behave like indipendent fermions at the temperature 0 K, with the cells independent of one another. The energy level of a particle in a three dimensional infinite well are given by the formula.

$$\epsilon(n_x, n_y, n_z) = \frac{h^3}{8ml^2}(n_x^2 + n_y^2 + n_z^2) \tag{3.4}$$

$$= \frac{h^3}{8ml^2}R^2 \tag{3.5}$$

Where $n_x, n_y, n_z = 1, 2, 3...$ and the second equality defines by the quantity R. For high quantum numbers, that is, for large R, the number of distinct energy levels with energy smaller than ϵ can be approximated by the volume of one octant of a spherical with radius R in the space n_x, n_y, n_z. This number is,

$$\phi(\epsilon) = \frac{1}{8}\left(\frac{4^3}{3}\right) \tag{3.6}$$

$$= \frac{\pi}{6}\left(\frac{8ml^2\epsilon}{h^2}\right)^{\frac{3}{2}} \tag{3.7}$$

The number of energy levels between ϵ and $\epsilon+\delta\epsilon$ is accordingly

$$g(\epsilon)\Delta\epsilon = \phi(\epsilon + \delta\epsilon) - \phi(\epsilon) \tag{3.8}$$

$$= \frac{\pi}{4}\left(\frac{8ml^2\epsilon}{h^2}\right)^{\frac{3}{2}} \epsilon^{\frac{1}{2}} + \phi(\delta\epsilon)^2 \tag{3.9}$$

where the function $g(\epsilon)$ is the density of states at energy ϵ. To compute the total energy for the cell with electrons, we need the probability for the state with energy to be occupied which we call $f(\epsilon)$. This is the Fermi Dirac distribution.

$$f(\epsilon) = \frac{1}{1 + \exp^{\beta(\epsilon-\mu)}} \tag{3.10}$$

where ϵ_f is the Fermi energy. All the states energy smaller than ϵ_f are occupied and those with energy greater than ϵ_f are occupied. The Fermi energy ϵ_f is the zero temperature limit of the chemical potential μ. Now we find the total energy of the electrons in this cell by summing the contributions from the different energy states:

$$\Delta E = 2\int \epsilon f(\epsilon) g(\epsilon) d\epsilon \tag{3.11}$$

$$= 2\int \epsilon f(\epsilon) \frac{\pi}{4}\left(\frac{8ml^2}{h^2}\right)^{\frac{3}{2}} \epsilon^{\frac{1}{2}} d\epsilon \tag{3.12}$$

$$= \frac{8\pi}{5}\left(\frac{2m}{h^2}\right)^{\frac{3}{2}} l^3 \epsilon_f^{\frac{5}{2}} \tag{3.13}$$

where the factor 2 enters because each energy level is doubly occupied by one electron with spin and another with spin β. The fermi energy E_f is related to the number of electrons ΔN in the cell through the formula,

$$\begin{aligned} \Delta N &= 2\int f(\epsilon)g(\epsilon)d\epsilon \\ &= \frac{8\pi}{3}\left(\frac{2m}{h^2}\right)^{\frac{3}{2}} l^3 {\epsilon_f}^{\frac{3}{2}} \end{aligned} \tag{3.14}$$

Eleminating ϵ_f from 3.13 and 3.14 we have,

$$\Delta E = \frac{3}{5}\Delta N E_f \tag{3.15}$$

$$= \frac{3h^2}{10m}\left(\frac{3}{8\pi}\right)^{\frac{2}{3}} l^3 \left(\frac{\Delta N}{l^3}\right)^{\frac{5}{3}} \tag{3.16}$$

Equation(3.16) is a relation between total kinetic energy and the electron density $n = \frac{\Delta N}{l^3} = \frac{\Delta N}{\Delta V}$ for each cell in the space. Adding the contribution from all cells we find the total kinetic energy to be, now reverting to atomic units,

$$T_{TF}[n] = C_f \int n^{\frac{5}{3}}(\vec{r})d\vec{r} \tag{3.17}$$

Where

$$C_f = \frac{3}{10}(3\pi^2)^{\frac{2}{3}} = 2.871 \tag{3.18}$$

Here, we first come across the LDA [60] one of the most significant concepts in contemporary density functional theory. By using locally applicable relations suited for a homogeneous electronic system, electronic characteristics are approximated as functions of the electron density. In terms of electron density, the energy formula for an atom is

$$T_{TF}[n(\vec{r})] = C_F \int n^{\frac{5}{3}}(\vec{r})d\vec{r} - Z\int \frac{n(\vec{r})}{\vec{r}}d\vec{r} + \frac{1}{2}\int\int \frac{n(\vec{r_1})n(\vec{r_2})}{|\vec{r_1} - \vec{r_2}|}d\vec{r_1}d\vec{r_2} \tag{3.19}$$

This is the energy functional of Thomas-Fermi theory of atoms. The method became considered as an overly simplified model of little real significance for quantitative

predictions in atomic, molecular, or solid state physics because the accuracy for atoms is not as high with this model as it is with other methods.

3.4 The Hohenberg-Kohn (HK) theorems

Density functional theory (DFT) is the most widely used many-body approach for electronic structure calculations and has significantly impacted on modern science and engineering. DFT is made possible by the existance of two ingeniously simple theorems put forward and proven by Hohenberg and Kohn in 1964. The Hohenberg-Kohn theorems which have become a basic tool for the study of electronic structure of matter. Basically, any system that involves electron.

3.4.1 The HK theorem I

For any system of interacting particles in an external potential $V_{ext}(\vec{r})$, the density is uniquely determined (in other words, the external potential is a unique functional of the density).

Proof of the HK theorem I

Assume that there exist two potentials $V_{ext}(\vec{r})$ and $V'_{ext}(\vec{r})$ differing by more than a constant and giving rise to the same ground state density, $n_0(\vec{r})$. Obviously, $V_{ext}(\vec{r})$ and $V'_{ext}(\vec{r})$ belong to distinct Hamiltonians $\hat{H}$ and $\hat{H}'$, which give rise to distinct wave functions ψ and ψ'. Because of the variational principle, no wave function can give an energy that is less than the energy of ψ for $\hat{H}$. That is

$$\begin{aligned} E_0 &< \langle \psi' | \hat{H} | \psi' \rangle \\ &< \langle \psi' | \hat{H}' | \psi' \rangle + \langle \psi' | \hat{H} - \hat{H}' | \psi' \rangle \\ &< E'_0 + \int n_0(\vec{r}) [V_{ext}(\vec{r}) - V'_{ext}(\vec{r})] d\vec{r} \end{aligned} \tag{3.20}$$

Similarly

$$\begin{aligned} E_0' &< \langle\psi|\hat{H}|\psi\rangle \\ &< \langle\psi|\hat{H}|\psi\rangle + \langle\psi|\hat{H}' - \hat{H}|\psi\rangle \\ &< E_0 + \int n_0(\vec{r})[V_{ext}'(\vec{r}) - V_{ext}(\vec{r})]d\vec{r}. \end{aligned} \tag{3.21}$$

Adding eq.(3.20) and eq.(3.21) lead to the contradiction

$$E_0 + E_0' < E_0 + E_0' \tag{3.22}$$

which is clearly a contradiction. Thus, the theorem has been proven by reduction absurdum.

3.4.2 The HK theorem II

A universal functional $F[n(\vec{r})]$ for the energy $E[\psi']$ can be defined in terms of the density, The exact ground state is the global minimum value of this functional.

Proof of the HK theorem II

Since the external potential is uniquely determined by the density and since the potential in turn uniquely (except in degenerate situations) determines the ground state wavefunction, all the other observables of the system such as kinetic energy are uniquely determined. Then one may write the energy as a functional of the density. The universal functional $F[n(\vec{r})]$ can be written as

$$F[n(\vec{r})] \equiv T[n(\vec{r})] + E_{int}[n(\vec{r})] \tag{3.23}$$

where $T[n(\vec{r})]$ is the kinetic energy and $E_{int}[n(\vec{r})]$ is the interaction energy of the particles. According to variational principle, for any wavefunction ψ', the energy functional $E[\psi']$:

$$E[\psi'] \equiv \langle\psi'|\hat{T} + \hat{V}_{int} + \hat{V}_{ext}|\psi'\rangle \tag{3.24}$$

has its global minimum value only when ψ' is the ground state wavefunction ψ_0 with the constraint that the total number of the particle is conserved. According to HK theorem I, ψ' must correspond to a ground state with particle density $n'(\vec{r})$

and external potential $V'_{ext}(\vec{r})$, then $E[\psi']$ is a functional of $n'(\vec{r})$. According to variational principle:

$$\begin{aligned} E[\psi'] &\equiv \langle\psi'|\hat{T} + \hat{V}_{int} + \hat{V}_{ext}|\psi'\rangle \\ &= E[n'(\vec{r})] \\ &= \int n'(\vec{r})V'_{ext}(\vec{r})d\vec{r} + F[n'(\vec{r})] \\ &> E[\psi_0] \\ &= \int n_0(\vec{r})V_{ext}(\vec{r})d\vec{r} + F[n_0(\vec{r})] \\ &= E[n_0(\vec{r})] \end{aligned} \tag{3.25}$$

Thus the energy functional $E[\psi'] \equiv \int n(\vec{r})V_{ext}(\vec{r})d\vec{r} + F[n(\vec{r})]$ evaluated for the correct ground state density $n_0(\vec{r})$ is indeed lower than the value of this functional for any other density $n(\vec{r})$. Therefore by minimizing the total energy functional of the system with respect to variations in the density $n(\vec{r})$, one would find the exact ground state density and energy. This functional only determines ground state properties, it doesn't provide any guidance concerning excited states.

3.5 Kohn-Sham (KS) equation

An inventive indirect method of monoelectronic equation for the kinetic-energy functional $T[n(\vec{r})]$ was developed by Kohn and Sham in 1965 as Kohn-Sham (KS) method. Kohn and Sham proposed introducing orbitals into the problem in such a way that the kinetic energy can be computed simply to good accuracy, leaving a small residual correction that is handled separately. It is convenient to begin with the exact formula for the ground-state kinetic energy,

$$T = \sum_{i}^{N} a_i \langle\psi_i| - \frac{1}{2}\nabla^2|\psi_i\rangle \tag{3.26}$$

where, ψ_i and a_i respectively, natural spin orbitals and their occupation numbers. We are assured from the Hohenberg-Kohn theory that this T is a functional of the

total electron density.

$$n(\vec{r}) = \sum_{i}^{N} a_i |\psi_i(\vec{r})|^2 \tag{3.27}$$

Kohn and Sham showed that one can built a theory using simpler formulas, namely,

$$T_s[n] = \sum_{i}^{N} \langle \psi_i | -\frac{1}{2}\nabla^2 | \psi_i \rangle \tag{3.28}$$

and

$$n(\vec{r}) = \sum_{i}^{N} |\psi_i(\vec{r})|^2 \tag{3.29}$$

This representation of kinetic energy and density holds true for the determinantal wave function that exactly describes N non-interacting electrons. In analogy with the Hohenberg-Kohn defination of the universal functional $F_{HK}[n]$, Kohn and Sham invoked a corresponding non-interacting reference system, with the Hamiltonian,

$$\hat{H}_s = \sum_{i}^{N} (\frac{1}{2}\nabla_i^2) + \sum_{i}^{N} \nu_s(\vec{r}) \tag{3.30}$$

in which there are no electron-electron repulsion terms and for which the ground state electron energy is exactly n. For this system, there will be an exact determinantal ground-state wave function,

$$\psi_s = \frac{1}{\sqrt{N!}} det[\psi_1 \psi_2 \dots \psi_N] \tag{3.31}$$

where ψ_i are the N lowest eigenstates of the one-electron Hamiltonian $\hat{h}_s$:

$$\hat{h}_s \psi_i = [-\frac{1}{2}\nabla^2 + \nu_s(\vec{r})]\psi_i = \epsilon_{me}\psi_i \tag{3.32}$$

The kinetic energy is $T_s(n)$ given by eq.(3.28).

$$T_s[n] = \langle \psi_s | \sum_{i}^{N} (-\frac{1}{2}\nabla_i^2) | \psi_i \rangle = \sum_{i=1}^{N} \langle \psi_i | -\frac{1}{2}\nabla^2 | \psi_i \rangle \tag{3.33}$$

The quantity $T_s[n]$, although uniquely defined for any density, is still not the exact kinetic energy functional. Kohn-Sham set up a problem of interest in such a way

that $T_s[n]$ is it's kinetic energy component. To produce the desired separation out of $T_s[n]$ as the kinetic energy component, we write the equation as

$$F[n] = T_s[n] + J[n] + E_{xc}[n]. \tag{3.34}$$

Where

$$E_{xc}[n] = T[n] - T_s[n] + V_{ee}[n] - J[n] \tag{3.35}$$

Here the quantity $E_{xc}[n]$ is called exchange-correlation energy. It contains the difference between T and T_s and non-classical part of $V_{ee}[n]$. The Euler equation becomes

$$\mu = \nu_{eff}(\vec{r}) + \frac{\delta T_s[n]}{\delta n(\vec{r})} \tag{3.36}$$

Where KS effective potential is defined by

$$\begin{aligned} \nu_{eff}(\vec{r}) &= \nu(\vec{r}) + \frac{\delta J[n]}{\delta n(\vec{r})} + \frac{\delta Exc[n]}{\delta n(\vec{r})} \\ &= \nu(\vec{r}) + \int \frac{n(\vec{r}')}{|\vec{r} - \vec{r}'|} dr' + \nu_{xc}(\vec{r}) \end{aligned} \tag{3.37}$$

with the exchange-correlation potential

$$\nu_{xc}(\vec{r}) = \frac{\delta E_{xc}[n]}{\delta n(\vec{r})} \tag{3.38}$$

For a system of non-interacting electrons moving in the external potential $\nu_s(\vec{r}) = \nu_{eff}(\vec{r})$. Therefore, for a given $\nu_{eff}(\vec{r})$, one obtains the $n(\vec{r})$ that satisfies eq.(3.38) simply by solving the N-one electron equations,

$$[-\frac{1}{2}\nabla^2 + \nu_{eff}(\vec{r})]\psi_i = \epsilon_{me}\psi_i \tag{3.39}$$

where ϵ_{me} is the eigenvalue of monoelectron equation and setting

$$n(\vec{r}) = \sum_i^N |\psi_i(\vec{r})|^2 \tag{3.40}$$

Eq.(3.37) and eq.(3.40) are celebrated Kohn-Sham equations.

The Kohn-Sham equations derived above that are summerized in the flow chart in Figure 3.1. They are a set of Schrödinger like independent particle equations which must be solved subject to the condition that the effective potential ν_{eff} and the density $n(\vec{r})$ are consistent. After solving Kohn-Sham equations, we will have a set of single electron wave functions. These wave functions can be used to calculate the new electron density. As an input, the new electron density is fed into the next cycle. Finally, after each iteration, compare the differences in calculated electron densities. If the difference in electron density between consecutive iterations is less than a suitably determined convergence threshold, the solution of the Kohn-Sham equations is deemed self-consistent. The predicted electron density has now been converted to the ground state electron density, which can be used to compute the total energy of the system.

3.5.1 Solving Khon-Shan equation

In a condensed matter system the KS equation gives a way to obtain the exact density and energy of the ground state. The process starts with an initial electron density n(r), usually a superposition of atomic electron density, then the effective KS potential ν_{eff} is calculated and the KS equation is solved with single particle eigenvalues and wave functions, a new electron density is then calculated from the wave functions. This is usually done numerically through some self consistent iteration as shown in above flowchart. Self-consistent condition can be the change of total energy or electron density from the previous iteration or total force acting on atoms is less than some chosen small quantity, or a combination of these individual conditions. If the self-consistency is not achieved, the calculated electron density will be mixed with electron density from previous iterations to get a new electron density. A new iteration will start with the new electron density. This process continues until selfconsistency is reached. After the self-consistency is reached, various quantities can be calculated including total energy, forces, stress, eigenvalues, electron density of states, band structure, etc..

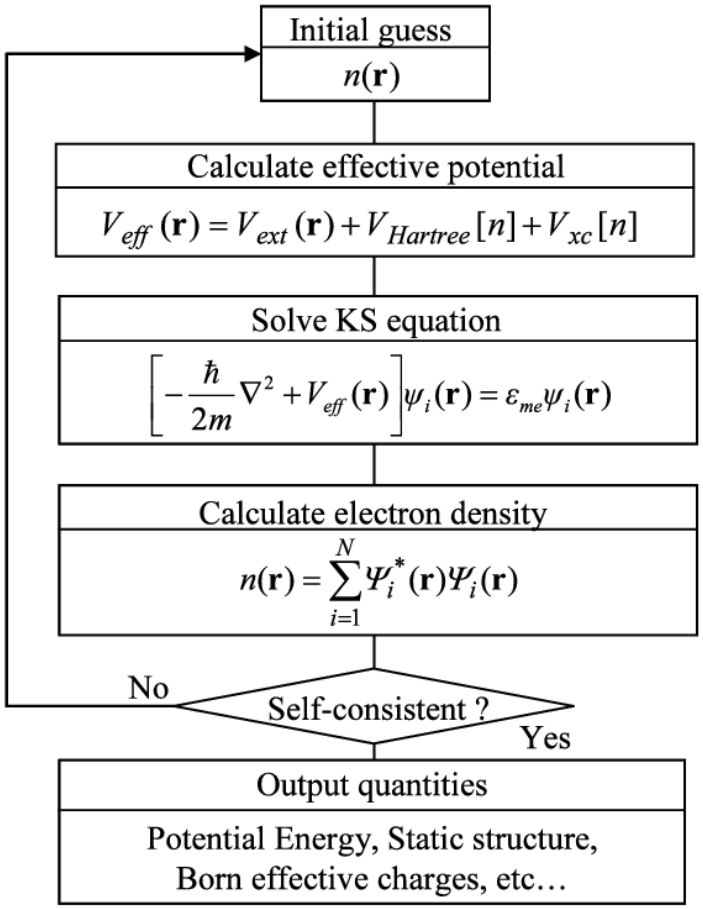

Figure 3.1: Flowchart of self-consistency loop for solving Kohn-Sham equation

3.6 The exchange-correlation (XC) functional

The exchange-correlation functional is at the core of density functional theory (DFT) that determines the accuracy of DFT in describing the interactions among electrons/ions in solids and molecules. The crucial quantity in the Kohn-Sham approach is the exchange-correlation energy which is expressed as a functional of the density $E_{xc}[\vec{n}]$. The exchange-correlation potential for a homogeneous electron gas (HEG) at the electron density observed at position $\vec{r}$. This approximation uses only the local density to define the approximate exchange-correlation functional, hence called local density approximation (LDA) and widely used

$$\begin{aligned} E_{xc}^{LDA}(\vec{r}) &= \int n(\vec{r}\epsilon)_{xc}^{hom} n(\vec{r}) d\vec{r} \\ &= \int [n(\vec{r}\epsilon)_{x}^{hom} n(\vec{r}) + n(\vec{r}\epsilon)_{c}^{hom} n(\vec{r})] d\vec{r} \\ &= E_{xc}^{LDA}[n(\vec{r})] \end{aligned} \tag{3.41}$$

The LDA is very simple, corrections to the exchange-correlation energy due to the inhomogeneities in the electronic density are ignored. Because of exchange-correlation energy of inhomogeneous charge density can significantly different from HEG result. This leads to development of various generalized-gradient approximation (GGA). In the GGA approximation, the local electron density and local gradient in the electron density are included in the exchange and correlation energies. One example of GGA functional used in DFT is the Perdew-Burke Ernzerhof (PBE) functional. It is formulated as

$$E_{xc}^{PBE} = E_{xc}^{LDA} + E_{c}^{PBE}. \tag{3.42}$$

Where, E_{xc}^{PBE} is the exchange correlation energy calculated using the PBE functional. E_{xc}^{LDA} is the exchange correlation energy calculated using LDA approximation and E_{c}^{PBE} is the correlation energy term specific to the PBE functional.

The exchange correlation potential was solved by GGA functional that understimates tha band gap value. Therefore, the modified Becke-Johnson exchange potential and LDA correlation by Trans and Blaha in 2009 (TB-mBJ) allows the calculation of band gaps with an accuracy similar to very expensive GW calculations.

3.7 Local Density Approximation (LDA)

The Khon Sham equation while exactly incorporating the kinetic energy $T_s[n]$, still leave the exchange correlational functional $E_{xc}[n]$ unsetteled. In Khon Sham equation let us introduce the local density approximation proposed by Khon and Sham. The kinetic energy $T_s[n]$ is regorously treated in the Kohn Sham schame, we can use the uniform electron gas formula solely for the unknown part of the rest of the energy functional. Thus we introduce the local density approximation (LDA) for exchange and correlation energy.

$$E_{xc}^{PBE}[n] = \int n(\vec{r})\epsilon_{xc}(n)d\vec{r} \tag{3.43}$$

Where $\epsilon_{xc}[n]$ indicates the exchange and correlation energy per particle of a uniform electron gas of density n. The corresponding exchange correlation potential then

becomes,

$$\begin{aligned} V_{xc}^{LDA}(\vec{r}) &= \frac{E_{xc}^{PBE}[n]}{\delta n(\vec{r})} \\ &= \epsilon_{xc}(n(\vec{r})) + n(\vec{r})\frac{E_{xc}[n]}{\delta n(\vec{r})} \end{aligned} \tag{3.44}$$

and the Khon Sham equations read, This self consistent solution defines the KS local density approximation, which is the literature is usually simply called Local Density Approximation (LDA) method. The function $\epsilon_{xc}[n]$ can be devided into exchange and correation contributions,

$$\epsilon_{xc}(n) = \epsilon_x(n) + \epsilon_c(n) \tag{3.45}$$

The exchange part is already known given by the Dirac exchange energy functional.

$$\epsilon_x(n) = -C_x n^{\frac{1}{3}}(\vec{r}) \tag{3.46}$$

where

$$C_x = \frac{3}{4}(\frac{3}{\pi})^{\frac{1}{3}} \tag{3.47}$$

3.8 Local Spin Density Approximation (LSDA)

The spin density functional theory is the necessary generalization for systems in the presence of an external magnetic field. It is also exceedingly important for systems in the absence of a magnetic field, because it allows one to build more physics into the approximate exchange-correlation functional through its spin dependence. In the presence of a magnetic field $B(\vec{r})$ that acts only on the spins of the electrons, the Hamiltonian of the system becomes,

$$H = -\frac{1}{2}\sum_{i}^{N}\nabla_i^2 + \sum_{i}^{N}V(\vec{r}) + \sum_{i<1}^{N}\frac{1}{\vec{r_{ij}}} + 2\beta_e\sum_{i}^{N}B(\vec{r}).\vec{S_i} \tag{3.48}$$

Where, $\beta_e = \frac{e\hbar}{2mc}$ is the Bohr magneton and $\vec{S_i}$ is the electron angular momentum vectorfor the $i^{t\hbar}$ electron. The added magnetic interaction is still a one electron operator, just like the nuclear potential $V(\vec{r})$. We can combine terms in the following

convenient way:

$$\hat{V} = \sum_{i}^{N} V(\vec{r_i}) + 2\beta_e \sum_{i}^{N} B(\vec{r}).\vec{S_i} \tag{3.49}$$

$$= \int v(\vec{r})\hat{n}(\vec{r})d\vec{r} - \int B(\vec{r})\hat{m}(\vec{r})d\vec{r} \tag{3.50}$$

where $\hat{n}(\vec{r})$ is the operator for electron density,

$$\hat{n}(\vec{r}) = \sum_{i}^{N} \delta(\vec{r} - \vec{r_i}) \tag{3.51}$$

and and $\hat{m}(\vec{r})$ is the operator for the electron magnetization density,

$$\hat{m}(\vec{r}) = -2\beta_e \sum_{i}^{N} S_i \delta(\vec{r} - \vec{r_i}) \tag{3.52}$$

Both $\hat{n}(\vec{r})$ and $\hat{m}(\vec{r})$ are local operators. The expectation value of $\hat{V}$ for the state $|\psi\rangle$ is given by,

$$\langle\psi|\hat{V}|\psi = \int v(\vec{r})n(\vec{r})d\vec{r} - \int B(\vec{r})m(\vec{r})d\vec{r} \tag{3.53}$$

where the electron density is given by,

$$n(\vec{r}) = \langle\psi|\hat{n}(\vec{r})|\psi\rangle \tag{3.54}$$

and the magnetization density by,

$$m(\vec{r}) = \langle\psi|\hat{m}(\vec{r})|\psi\rangle \tag{3.55}$$

We shall discuss only the simple case of z-direction $b(\vec{r})$. We then have,

$$\langle\psi|\hat{V}|\psi\rangle = \int v(\vec{r})n(\vec{r})d\vec{r} - \int b(\vec{r})m(\vec{r})d\vec{r} \tag{3.56}$$

where

$$\begin{aligned} m(\vec{r}) &= -2\beta_e\langle\psi| \sum_{i}^{N} S_z(i)\delta(\vec{r} - \vec{r_i})|\psi\rangle \\ &= \beta_e[n^{\beta}(\vec{r}) - n^{\alpha}(\vec{r})] \end{aligned} \tag{3.57}$$

We obtain the spin density functional theory by breaking the minimum search for the ground-state energy into two steps. Namely,

$$E_0 = \min_{\psi}\langle\psi|T + V_{ee} + \sum_{i}^{N} U(\vec{r_i}) + 2\beta_e \sum_{i}^{N} b(\vec{r_i}).S_z(i)|\psi\rangle \tag{3.58}$$

$$= \min_{n^\alpha, n^\beta}\{\min_{\psi\to n^\alpha, n^\beta}\langle\psi|T + V_{ee}\rangle + \int [v(\vec{r})n(\vec{r}) - \int b(\vec{r})m(\vec{r})]d\vec{r}\} \tag{3.59}$$

$$= \min_{n^\alpha, n^\beta}\{F[n^\alpha, n^\beta] + \int [(V(\vec{r}) - \beta_e b(\vec{r}))n^\alpha(\vec{r}) + \beta_e b(\vec{r}))n^\beta(\vec{r})]d\vec{r}\} \tag{3.60}$$

where

$$F[n^\alpha, n^\beta] = \min_{\psi\to n^\alpha, n^\beta}\langle\psi|T + V_{ee}|\psi\rangle \tag{3.61}$$

This provides constrained-search formulation of the universal functional $F[n^\alpha, n^\beta]$. The functional $F[n^\alpha, n^\beta]$ searches all ψ that yield the input $n^\alpha(\vec{r})$ and $n^\beta(\vec{r})$, then $F[n^\alpha, n^\beta]$ assumes the minimum of $\langle F + V_{ee}\rangle$. The last equality of (3.61) is the basis of the spin-density-functional theory: n^α and n^β are all that are needed to describe the ground state of the many-electron system in the presence of a magnetic field $b(\vec{r})$. However, $F[n^\alpha, n^\beta]$ is unknown, and approximation is necessary for the theory to be implemented. The Kohn-Sham method can now be introduced to rigorously handle the kinetic energy contribution to $F[n^\alpha, n^\beta]$,

$$F[n^\alpha, n^\beta] = T_s[n^\alpha, n^\beta] + J[n^\alpha + n^\beta] + E_{xc}[n^\alpha, n^\beta] \tag{3.62}$$

where $T_s[n^\alpha, n^\beta]$ is the Kohn-Sham kinetic-energy functional corresponding to a system of non-interacting electrons with densities n^α and n^β and $E_{xc}[n^\alpha, n^\beta]$ is the exchange correlation energy functional. A constrained search definition of T_s can also be given,

$$T_s[n^\alpha, n^\beta] = min\sum_{i\alpha} n_{i\alpha}\int d\vec{r}\phi^*_{i\alpha}(\vec{r})(\frac{1}{2}\nabla^2)\phi_{i\alpha}\vec{r} \tag{3.63}$$

where the minimization is over the set of $n_{i\alpha}$ and $\phi_{i\alpha}$, with constraints,

$$\sum_i n_{i\alpha}|\phi_{i\alpha}(\vec{r})|^2 = n^\alpha(\vec{r}) \tag{3.64}$$

$$\sum_i n_{i\beta}|\phi_{i\beta}(\vec{r})|^2 = n^\beta(\vec{r}) \tag{3.65}$$

We may express the energy (3.55) as a functional of the orbitals $\phi_{i\alpha}$,

$$\begin{aligned} E[n^\alpha, n^\beta] = \sum_{i\alpha} n_{i\alpha} \int d\vec{r}\phi^*_{i\alpha}(\vec{r})(-\frac{1}{2}\nabla^2)\phi_{i\alpha}\vec{r} + J[n^\alpha + n^\beta] + E_{xc}[n^\alpha, n^\beta] \\ + \int [(V(\vec{r}) + \beta_e b(\vec{r}))n^\alpha(\vec{r}) + (V(\vec{r}) - \beta_e b(\vec{r}))n^\beta(\vec{r})]d(\vec{r}) \end{aligned} \tag{3.66}$$

The variational search for the minimum of $E[n^\alpha, n^\beta]$ can then be carried out through orbitals, subject to normalization constraints,

$$\int \phi^*_{i\alpha}(\vec{r})\phi_{i\alpha}(\vec{r})d\vec{r} = 1 \tag{3.67}$$

The resulting Kohn-Sham equations are,

$$\hat{h}^\alpha_{eff}\phi_{i\alpha}(\vec{r}) = [-\frac{1}{2}\nabla^2 + V^\alpha_{eff}]\phi_{i\alpha}(\vec{r}) = \epsilon_{i\alpha}\phi_{i\alpha}(\vec{r}) \tag{3.68}$$

and

$$\hat{h}^\beta_{eff}\phi_{j\beta}(\vec{r}) = [-\frac{1}{2}\nabla^2 + V^\beta_{eff}]\phi_{j\beta}(\vec{r}) = \epsilon_{j\beta}\phi_{j\beta}(\vec{r}) \tag{3.69}$$

where the spin dependent effective potentials are,

$$v^\alpha_{eff}(\vec{r}) = v(\vec{r}) + \int \frac{n(\vec{r})}{|\vec{r} - \vec{r'}|d\vec{r}} + \frac{\delta E_{xc}[n^\alpha, n^\beta]}{\delta n^\alpha(\vec{r})} + \beta_e b(\vec{r}) \tag{3.70}$$

$$v^\beta_{eff}(\vec{r}) = v(\vec{r}) + \int \frac{n(\vec{r})}{|\vec{r} - \vec{r'}|d\vec{r}} + \frac{\delta E_{xc}[n^\alpha, n^\beta]}{\delta n^\beta(\vec{r})} + \beta_e b(\vec{r}) \tag{3.71}$$

In equations (3.65) and (3.66), the number of electrons with α spin and β spin,

$$N^\alpha = \int n^\alpha(\vec{r})d\vec{r} \tag{3.72}$$

and

$$N^\beta = \int n^\beta(\vec{r})d\vec{r} \tag{3.73}$$

need also to be varried to achieve minimum total energy under the constraint,

$$N = N^{\alpha} + N^{\beta} \tag{3.74}$$

With the spin-polarized Kohn-Sham equations, the kinetic energy is handled exactly and only the exchange-correlation energy remains to be determined. The exchange-correlation contribution can be separated into exchange and correlation pieces,

$$E_{xc}[n^{\alpha}, n^{\beta}] = E_x[n^{\alpha}, n^{\beta}] + E_c[n^{\alpha}, n^{\beta}] \tag{3.75}$$

where the exchange part is defined as,

$$E_x[n^{\alpha}, n^{\beta}] = -\frac{1}{2}\int\int \frac{1}{\vec{r}_{12}}\{|n_1^{\alpha,\alpha}(\vec{r_1}, \vec{r_2})|^2 + |n_1^{\beta,\beta}(\vec{r_1}, \vec{r_2})|^2\} d\vec{r_1}\vec{r_2} \tag{3.76}$$

with

$$n_1^{\alpha,\alpha}(\vec{r_1}, \vec{r_2}) = \sum_i n_{i\alpha}\phi_{i\alpha}(\vec{r_1})\phi_{i\alpha}^*(\vec{r_2}) \tag{3.77}$$

$$n_1^{\beta,\beta}(\vec{r_1}, \vec{r_2}) = \sum_i n_{i\beta}\phi_{i\beta}(\vec{r_1})\phi_{i\beta}^*(\vec{r_2}) \tag{3.78}$$

The $n_{i\alpha}$ and $\phi_{i\alpha}$ are those giving the Kohn-Sham kinetic energy, they are determined by p^{α} and p^{β}.

$$E_x[n^{\alpha}, n^{\beta}] = \frac{1}{2}E_x[n^{\alpha}, n^{\alpha}] + \frac{1}{2}E_x[n^{\beta}, n^{\beta}] \tag{3.79}$$

$$= \frac{1}{2}E_x^0[2n^{\alpha}] + \frac{1}{2}E_x^0[2n^{\beta}] \tag{3.80}$$

where

$$E_x^0[n] = E_x[\frac{1}{2}n, \frac{1}{2}n] \tag{3.81}$$

The Dirac local density approximation (LDA) for exchange is for the spin-compensated case. Thus from above equations, we obtain the local spin-density approximation (LSDA) for the exchange energy functional,

$$E_x^{LSDA}[n^{\alpha}, n^{\beta}] = 2^{\frac{1}{3}}C_x \int [(n^{\alpha})^{\frac{4}{3}} + (n^{\beta})^{\frac{4}{3}}] d\vec{r} \tag{3.82}$$

3.9 Generalized Gradient Approximation (GGA)

The LDA neglects the inhomogeneties of the real charge density which could be very different from the HEG. The XC energy of inhomogeneous charge density can be significantly different from the HEG result. This leads to be the development of verious generalized-gradient approximations (GGA) which include density gradient corrections and higher spatial derivatives of the electron density and give better result than LDA in many cases. Three most widely used GGA's are the from proposed by Becke [73], Perdew et al. [74], Burke and Enzerhof [75]. The definition of the XC energy functional of GGA is the generalized form in the equation of LSDA to include corrections ,

$$E_{XC}^{LSDA}[n_{\downarrow}(r), n_{\uparrow}(r)] = \int n(r)\epsilon_{XC}^{hom}[n_{\downarrow}(r), n_{\uparrow}(r)]dr \tag{3.83}$$

Where XC energy density $\epsilon_{XC}^{hom}(n(r))$ is a function of the density alone and is composed into exchange energy density $\epsilon_{XC}^{hom}(n(r))$ and correlation energy density $\epsilon_{C}^{hom}(n(r))$. So thet the XC energy functional is decomposed into exchange energy function $E_{XC}^{LDA}(n(r))$ linearly. From density gradient $\nabla(\vec{r})$ as,

$$\begin{aligned} E_{XC}^{GGA}[n_{\downarrow}(r), n_{\uparrow}(r)] &= \int n(r)\epsilon_{XC}^{hom}[n_{\downarrow}(r), n_{\uparrow}(r), |\nabla\uparrow(r)|, |\nabla\downarrow(r)|, ...]dr \\ &= \int n(r)\epsilon_{X}^{hom}n(r)F_{XC}[n_{\downarrow}(r), n_{\uparrow}(r), |\nabla\uparrow(r)|, |\nabla\downarrow(r)|, ...]dr \end{aligned} \tag{3.84}$$

Where F_{XC} is dimensionless and $\epsilon_{XC}^{hom}n(r)$ is the exchange energy density of the unpolarized HEG. FXC can be decomposed linearly into exchange contribution F_{XC} = F_X + F_C. Generally GGA works better than LDA, in pridicting binding energy of molecules and bond length, crystal lattice constants, especially the system where charge density varried rapidly. In case of ionic crystall, GGA overcorrects LDA results where the lattice constants of LDA fit well than GGA. But in case of transition metal oxides and rare-earth element, both LDA and GGA perform badly. This drawback leads to approximations beyond LDA and GGA.

3.10 LDA+U method

Strongly correlated system usually contain transition metal or rare-earth metal ions with partially filled d or f shells. Because of the orbital-independent potentials in LSDA and GGA, they cannot properly describe such systems. The total energy in LSDA+U [76] method is given by,

$$E_{tot}^{LDA+U}[\rho_\sigma(r), n_\sigma] = E^{LSDA}[\rho_\sigma(r)] + E^{U}[n_\sigma] - E_{dc}[n_(r)] \tag{3.85}$$

where, σ = spin indexes $\rho(r)$ = electron density for spin- electrons n = density matrix of f or d electron for spin-σ electrons $E^{LSDA}[\rho_\sigma(r)]$ = standard LSDA energy functional $E^{U}[n(r)]$ = electron-electron coulomb interaction energy. The last term is double counting term which remove the average LDA energy contribution of d or f electrons from the LDA energy

$$E_{dc}[n_(r)] = \frac{1}{2}UN(N-1) - \frac{1}{2}J[N_\uparrow(N_\uparrow - 1) + N_\downarrow(N_\downarrow - 1)] \tag{3.86}$$

where, $N = N_\uparrow + N_\downarrow$. U and J are coulomb and exchange parameters. If exchange and non sphericity is neglected then,

$$E_{tot}^{LDA+U} = E_{LDA} + \frac{1}{2}U\sum_{i\neq 1} n_i n_j - \frac{1}{2}UN(N-1) \tag{3.87}$$

The orbital energies ϵ_i are derivative of above equation with respect to orbital occupations n_i : $For n_i = 1$, LDA orbital energiesare shifted by $-\frac{U}{2}$ and by $\frac{U}{2}$ and by for unoccupied orbitals($n_i = 0$), resulting the upper and lower Hubbard bands, which opens a gap at the Fermi energy in transition metal oxides. In case of double counting term, it has two different tretement: AMF and FLL. The former is most suitable for small U system [77] and the letter for large U system [78]. The energies for double counting is given by [79],

$$E_{dc}^{AMF} = \frac{1}{2}UN^2 - \frac{U+2lJ}{2l=1}\frac{1}{2}\sum_\sigma N_\sigma^2 \tag{3.88}$$

and

$$E_{dc}^{AMF} = \frac{1}{2}UN(N-1) - \frac{1}{2}J\sum_{\sigma} N_{\sigma}(N_{\sigma-1}) \tag{3.89}$$

where, $\frac{N}{2(2l+1)}$= average occupation of the correlated orbitals $\frac{N_{\sigma}}{2l+1}$= average occupation of a single spin of the correlated orbital.

Chapter 4

Results and Discussion

4.1 Computational details

In our calculation, to compute the optoelectronic, thermoelectric and mechanical properties of K_2YAgBr_6 under pressure we employed the full potential linearized augmented plane wave (FP-LAPW) method within the DFT implemented in WIEN2k code [80]. We optimized the lattice parameters of K_2YAgBr_6 in the simple cubic phase with space group $Fm\bar{3}m$ (225) by using Birch-Murnaghan's equation of state [81]. The band structures and density of states are calculated by using Perdew-Burke-Ernzerhof generalized gradient approximation (PBE-GGA) [82, 83]. In all the calculations, some of the parameters were kept constant in reciprocal lattices, such as the Gaussian factor $G_{max} = 16$ (a.u)$^{-1}$, and angular momentum vector $l_{max} = 10$. For non-overlapping spheres, the radii of the muffin-tin for all calculations are chosen to be 2.5, 1.9, 2.05, and 1.76 a.u. for K, Y, Ag and Br respectively. An additional parameter that is obtained by multiplying the cutoff parameter $K_{max}R_{MT} = 8$ was used, where K_{max} is the plane wave cut-off for reciprocal lattice vector and R_{MT} is the muffin-tin radius. The first Brillouin Zone was sampled by using the Monkhorst-Pack [84] method using the k-point mesh was set as $15 \times 15 \times 15$ and $20 \times 20 \times 20$ for electronic and optical computations respectively. The limit

of energy convergence for the iteration process was set to 10^{-5} Ry and the total charge are 10^{-4} e. In order to compute the elastic constants, we used the Charpin's technique as it is implemented in WIEN2k [85]. According to Charpin's method, the elastic behavior of a material with a perfectly cubic structure can be effectively characterized by three distinct elastic constants C_{11}, C_{12}, and C_{44}. Finally, The thermoelectric properties are computed using BoltzTraP code that employs rigid band approximation and classical Boltzmann transport theory [86].

4.2 Structural properties

The double peroveskite compound K_2YAgBr_6 has face-centered cubic structure with the space group $Fm\bar{3}m$ (225) of four atoms per unit cell. The crystal structure of K_2YAgBr_6 double perovskite is illustrated in Figure 4.1. The atomic position in the unit cell are K (0.25, 0.25, 0.25), Y (0, 0, 0), Ag (0.5, 0.5, 0.5) and Br (0.2475, 0, 0). The corresponding Wyckoff sites are 8c for K, 4a for Y , 4b for Ag and 24e for O. To find the optimized ground states of the considered material, the

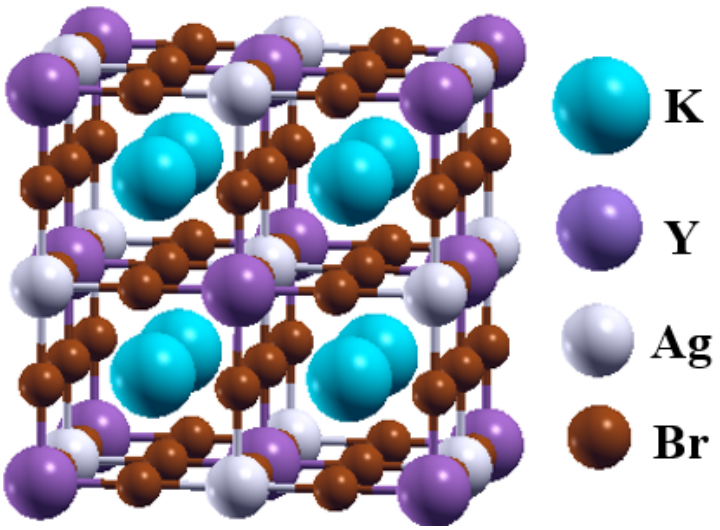

Figure 4.1: Schematics representation of the crystal structure of K_2YAgBr_6.

energy versus volume of a unit cell of the crystal was calculated, based on the Birch-Murnaghan's thermodynamic of state equation [87]. This graph determines the ground state energy corresponding to minimum volume, which provides information about the optimized lattice constant. The energy versus volume optimization curve

is presented in Figure 4.2. We investigate the variation of lattice parameters for K_2YAgBr_6 double perovskite under different hydrostatic pressures upto 150 GPa. The calculated lattice parameter at 0 GPa in this study exhibits very well consisten with previous work. The influence of applied hydrostatic pressure on lattice is exhibited from Table 4.1, it is observed that the values of lattice parameter decrease in a smooth way with increase of pressure, which implies that the space between atoms is getting reduced. As a result, repulsive influence between atoms become stronger, which conducts to the hardness of crystal compression under elevated pressure. The thermodynamic and structural stability can be estimated through

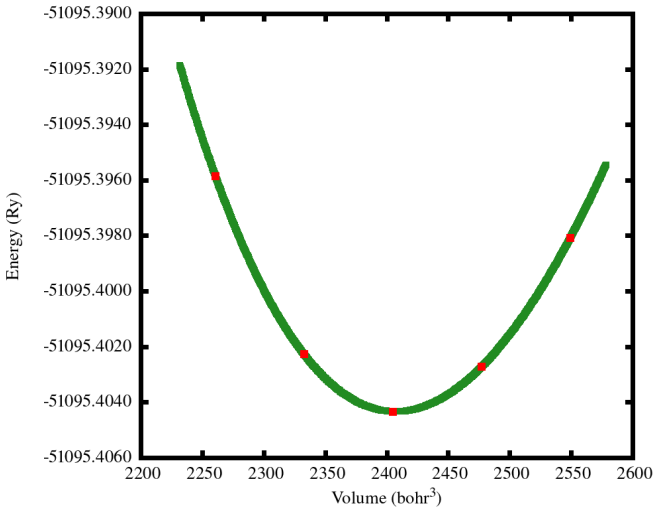

Figure 4.2: The calculated energy versus volume optimization curve of the K_2YAgBr_6 .

the enthalpy of formation (ΔH_f) eV and tolerance factor [88]. Statistical studies on double perovskites structure conducted by Li et al. [89,90], have revealed that for a stable double perovskite $0.71 < t_G < 1$. Moreover, it has been shown that $0.89 < t_G < 1$ refer to a perfectly stable cubic structure, while for those double perovskites with $0.71 < t_G < 0.89$, a tetragonal or an orthorhombic crystal structure is more probable [91]. For K_2YAgBr_6 the tolerance factor is found to be 0.94 [91] calculated by the equation;

$$\tau_G = \frac{R_K + R_{Br}}{\sqrt{2}(\frac{R_Y + R_{Ag}}{2} + R_{Br})} \tag{4.1}$$

Where R_K, R_{Br}, R_{Ag} and R_{Br} refer to the ionic radii of K, Y, Ag, Br atoms respectively. The thermodynamic stability of halide double perovskite can be checked by the expression given below:

$$\Delta H_f = E_{Total}(K_2YAgBr_6) - aE_K - bE_Y - cE_{Ag} - dE_{Br} \tag{4.2}$$

The factors E_{Total} (K_2YAgBr_6), aE_K, bE_Y, cE_{Ag}, dE_{Br} are the total energy and energy of the K atoms, along with energies of Y, Ag and Br atoms. The value of ΔH_f is -1.68 eV [91]. K_2YAgBr_6 is stable, as verified by negetive values of ΔH_f (eV). This means that during the formation of this compound, energy is released which stabilizes the product.

Table 4.1: Variation of lattice constants and band gaps of K_2YAgBr_6 under hydrostatic pressure up to 150 GPa

Pressures (GPa)	lattice constants (Å)		Band Gap(eV)	
	Our work	Other work	Our work	Other work
0	11.26	11.27[a]	3.07	3.3[a]
5	10.74	-	3.25	-
10	10.45	-	3.26	-
20	10.10	-	3.10	-
50	9.58	-	2.47	-
100	9.17	-	1.69	-
150	8.94	-	1.12	-

[a] *Ref.* [91]

4.3 Electronic properties

The electronic properties of the compound have been investigated in term of total, partial density of states (DOS) and energy band structure. These were calculated using PBE-GGA potential. The studied band structures of K_2YAgBr_6 at ambient pressure is demonstrated in Figure 4.3. The Fermi level is exhibited at zero of photon energy scale which is presented from -4 eV to $+4$ eV for all the samples. According to the band structure diagram, this compound has an indirect bandgap at L - Γ because the bands lie at different symmetry points, such as the valence band maximum (VBM) at L-point and the conduction band minimum (CBM) Γ with

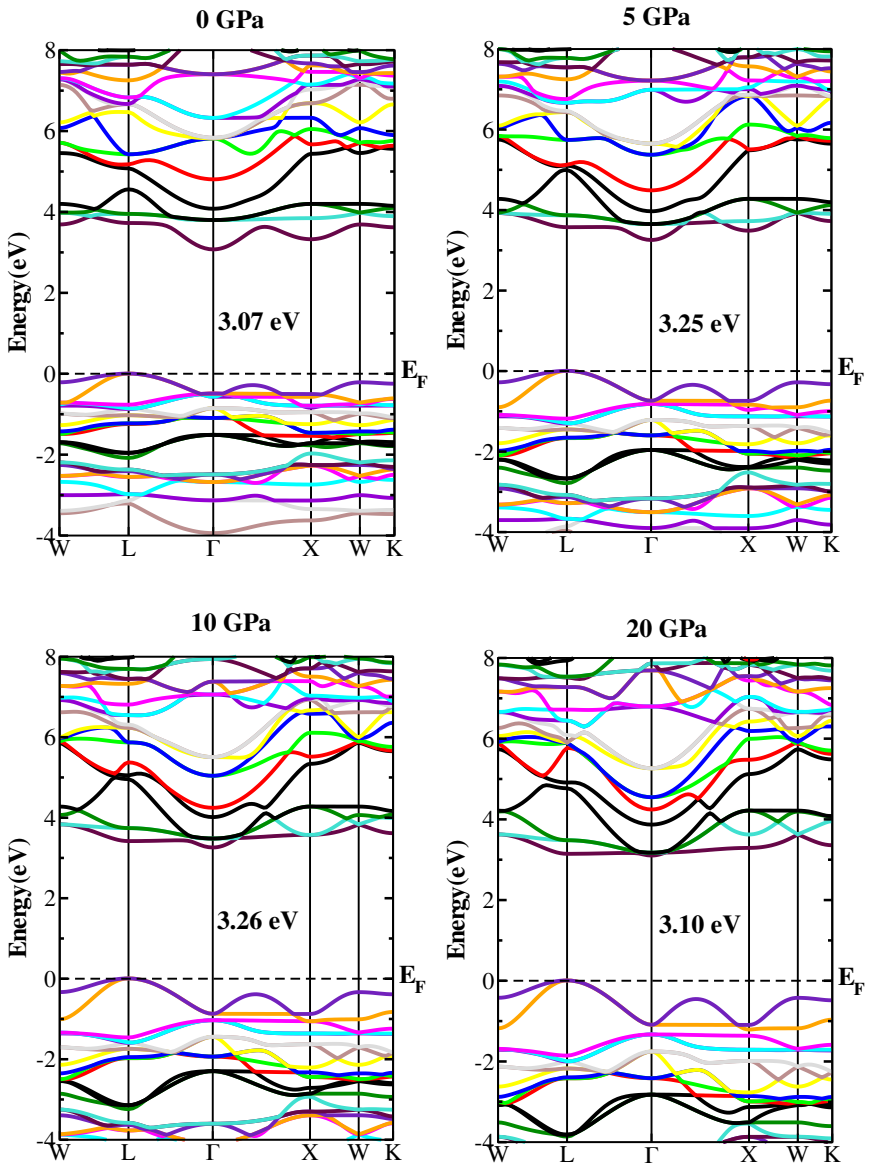

Figure 4.3: The calculated electronic band structure of K_2YAgBr_6 double perovskite under hydrostatic pressure up to 20 GPa.

values of 3.07 eV. It is evident that K_2YAgBr_6 is a wide band gap semiconductor. Figure 4.3 and 4.4 shows The studied band structures of K_2YAgBr_6 under variant pressures up to 150 GPa. The pressure is going up, the valance band maximum at L-point and the conduction band minimum at Γ-point start to shift toward E_F. As a result, the E_g of K_2YAgBr_6 decreases with pressure. As band gap of the K_2YAgBr_6 is reduced with increase of pressure, then the transition of excited electron becomes much more convenient and faster from valance band to conduction band. The K_2YAgBr_6 double perovskite has increasing affinity of absorption coefficient in

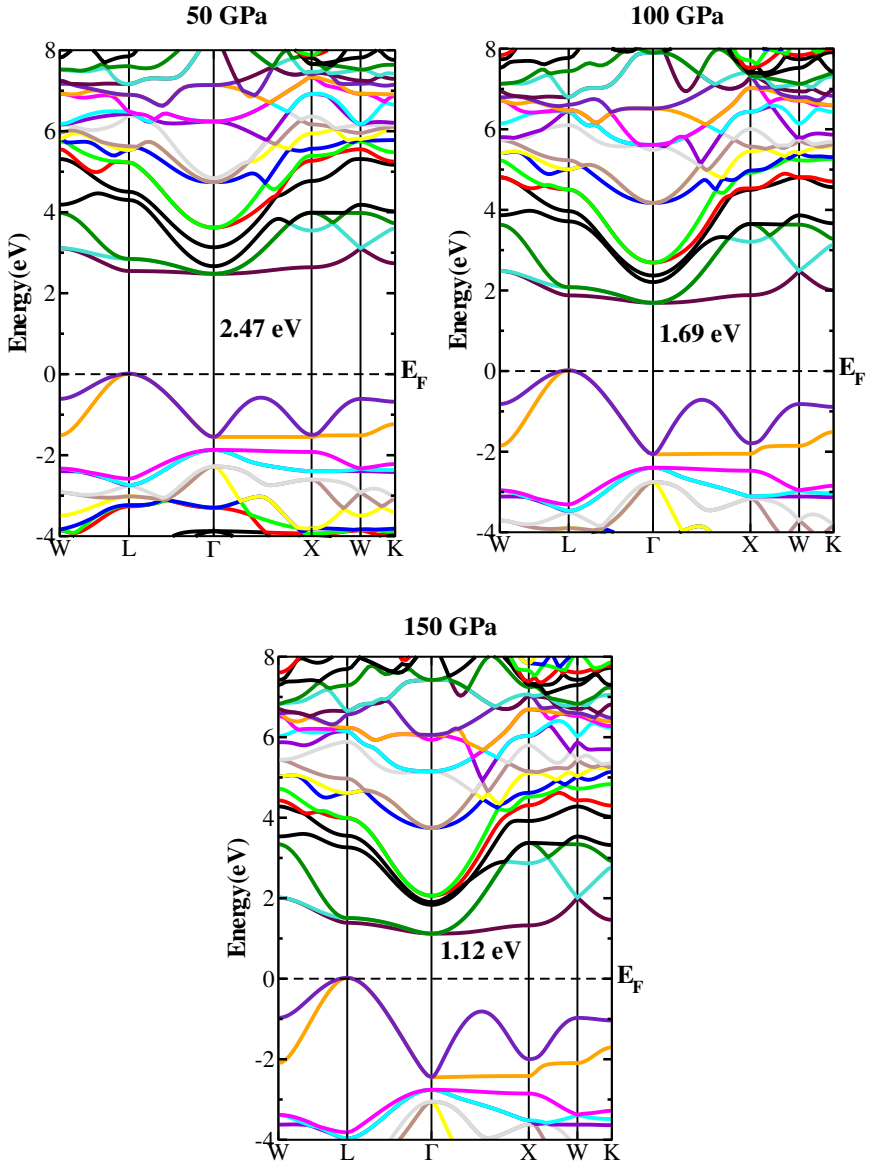

Figure 4.4: The calculated electronic band structure of K_2YAgBr_6 double perovskite under hydrostatic pressure up to 150 GPa.

the visible region with increasing applied hydrostatic pressure as depict in Figure 4.10. Under hydrostatic pressure, the band gap of the materials remain indirect under the cosidered range of pressure. To probe the contributing states in the band formation we plotted the total (TDOS) and partial density of states (PDOS) of K_2YAgBr_6 in the range -4 to $+4$, which are shown in Figure 4.5 at ambient pressure. The interband electronic transition depends upon the band structure and density of states which are involved in the formation of these bands. From the partial and total density of states, we can identify the electronic transitions between

VB, CB, and the hybridization between the different orbitals in the material. The

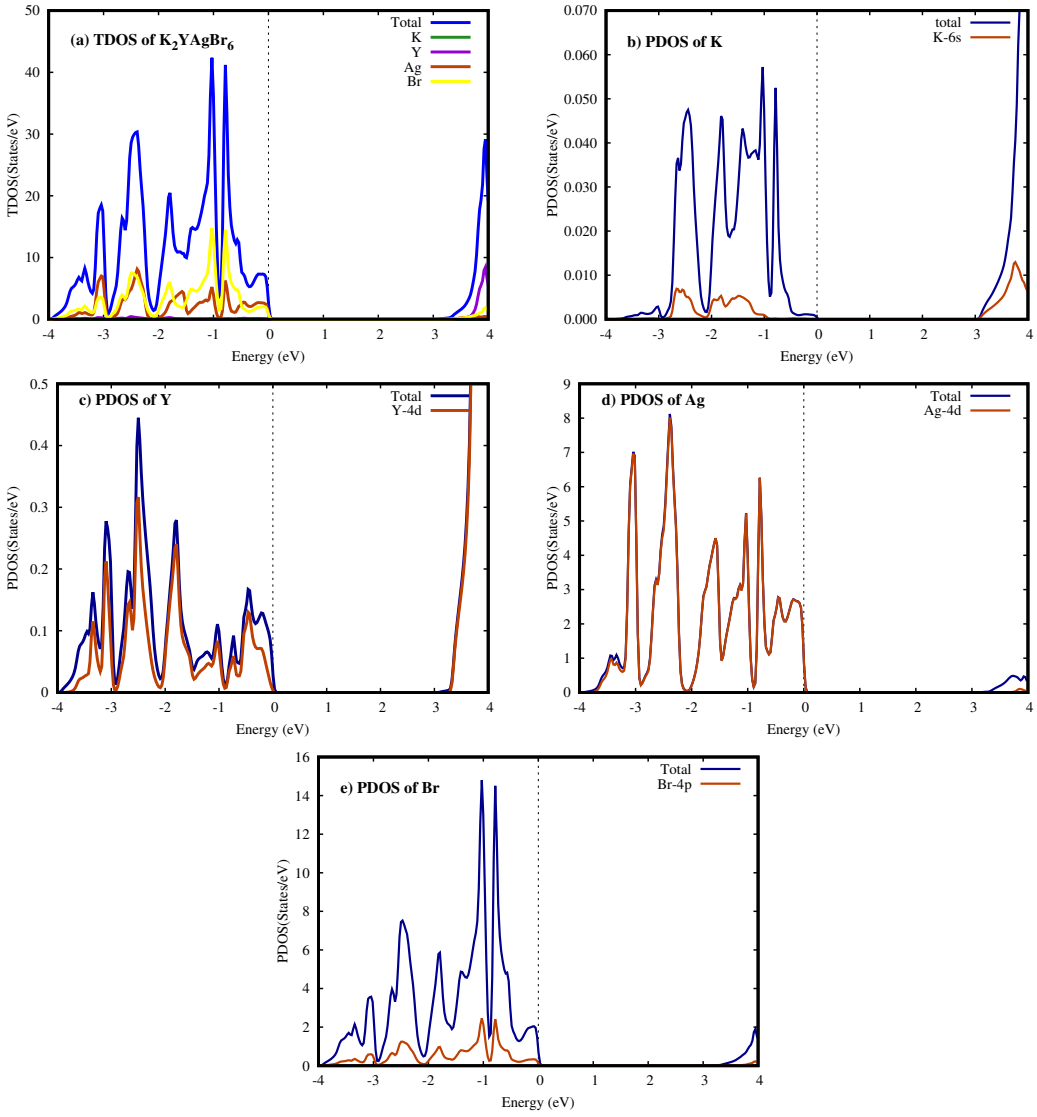

Figure 4.5: The total and partial density of states (PDOS) of b) K, c) Y, d) Ag and e) Br atoms in K_2YAgBr_6 at applied pressure.

region to the left of E_F shows valance band and region to the right of E_F represents conduction band. The plot of TDOS reveals that states in the valance band expand from -4 to 0 eV, while in the conduction band they lie In the formation of the VB, the energy states corresponding to 6s electrons of K meagerly, while energy states corresponding to 4d electrons of Ag and 4p electrons of Br take part significantly. However, in the conduction band, there is a major contribution of 4d states of K. We also investigated the changes in total density of states (TDOS) and partial density of states (PDOS) of K_2YAgBr_6 perovskite under several applied pressure is

plotted in Figure 4.6 and 4.7. As is evident in the total DOS plot that with the

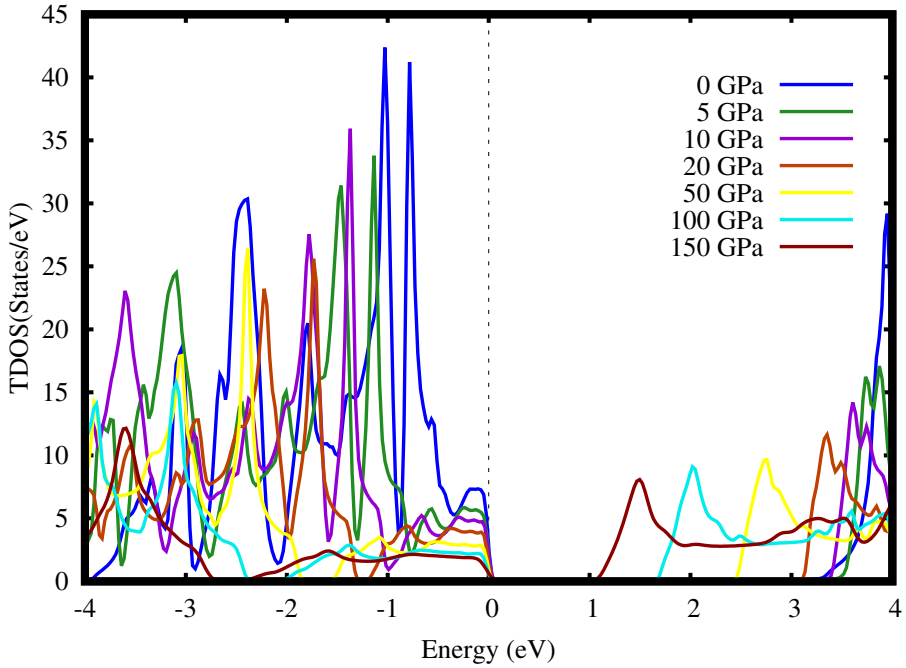

Figure 4.6: Total density of states of K_2YAgBr_6 at different pressure.

increase in pressure, the highest peak close to the top of the valence band exhibits an overall shift to the lower energy with continuously decreasing height. Moreover, at 150 GPa, an evident splitting in this peak appears indicating strong repulsive interaction between the states. Similarly, the bottom of the conduction band is shifted to the lower energy as the pressure increases, due to which, the band gap decreases that illustrates the pressure induced tuning of the optical properties can be expected. From the partial DOS plots, strong pd-hybridization among Ag-6p and K-6s states is evident. The strong pd-hybridization exerts more repulsive with pressure that increases the band gap. All the states illustrate that the increasing pressure from 0 to 150 GPa shifts the valence and conduction states to lower and lower energies, respectively, that decreases the band gap. It has been observed that the DOS at the Fermi level changes as the pressure changes. So the energy distance between the VB and CB from fermi level is also change. Similar to its behavior at 0 GPa, the K_2YAgBr_6 double perovskite demonstrates p-type semiconducting nature at all applied pressures.

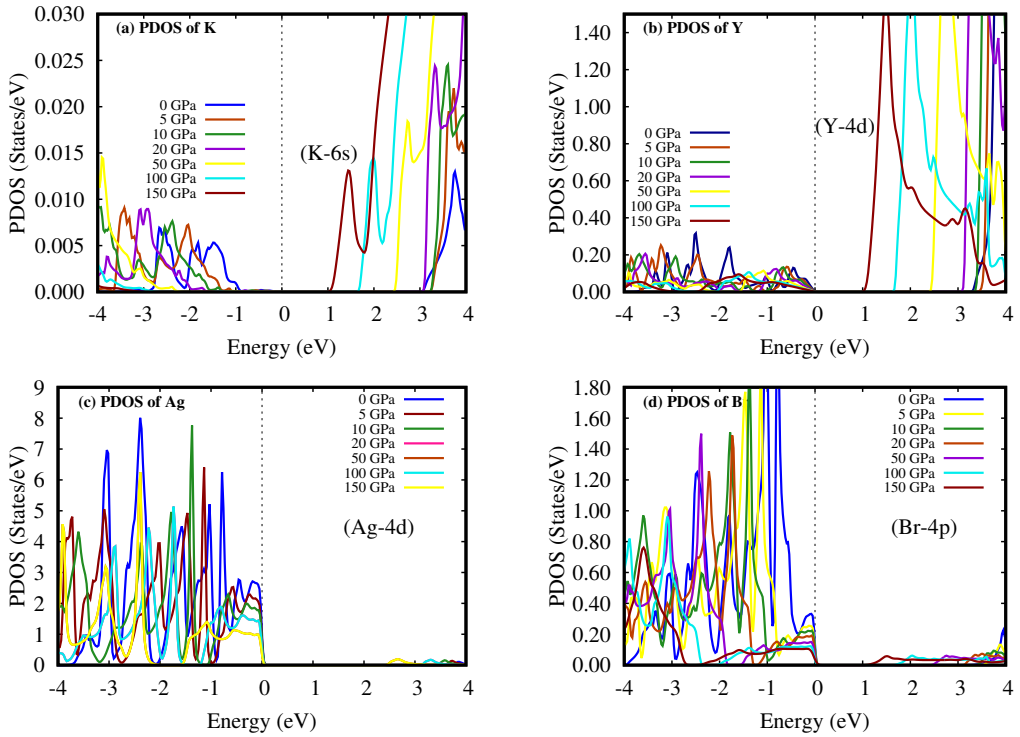

Figure 4.7: The partial density of states (PDOS) of b) K, c) Y, d) Ag and e) Br atoms in K_2YAgBr_6 at applied pressure.

4.4 Optical properties

The study of optical properties is very important fundamental approach to gain deep knowledge about the compatibility of material to better performance devices applications. Optical properties of a material define how it interacts with light. The response to electromagnetic radiation is important for optoelectronic device and solar cell applications in visible region [92]. Therefore, in this current work we have investigated the crucial optical properties such as dielectric function, absorption coefficient, optical conductivity, optical reflectivity and refractive index of K_2YAgBr_6 double perovskite in details under various hydrostatic pressure up to 150 GPa. Calculating these optical properties of double perovskite material under pressure helps us understand how their light interaction changes.

4.4.1 Dielectric function

To describe the absoption and dispersion ability of a material, it is necessary to calculate the frequency dependent complex dielectric function of compound $\epsilon(\omega) =$

$\epsilon_1(\omega) + i\epsilon_2(\omega)$, Where, $\epsilon_1(\omega)$ and $\epsilon_2(\omega)$ are represents real and imaginary parts of the dielectric function [93]. The real part describes the ability of the material to store energy in an electromagnetic field, while the imaginary part describes the loss of energy due to absorption or scattering by the material. The imaginary $\epsilon_2(\omega)$ with cubic symmetry substance [94]:

$$\epsilon_2(\omega) = \frac{e^2 h'}{\pi m^2 \omega^2} \Sigma_{\nu,c} \int_{BZ} |M_{c\nu}(k)|^2 \delta[\omega_{c\nu}(k) - \omega] d^3k \tag{4.3}$$

where $M_{cv}(\mathrm{k}) = \langle u_{ck}|e\nabla|u_{vk}\rangle$ is dipole matrix element expressing all the contributing electronic transitions. The real part $\epsilon_1(\omega)$ is computed using Kramers-Kronig relation [95, 96]. The static peak of dielectric function is an efficient parameter

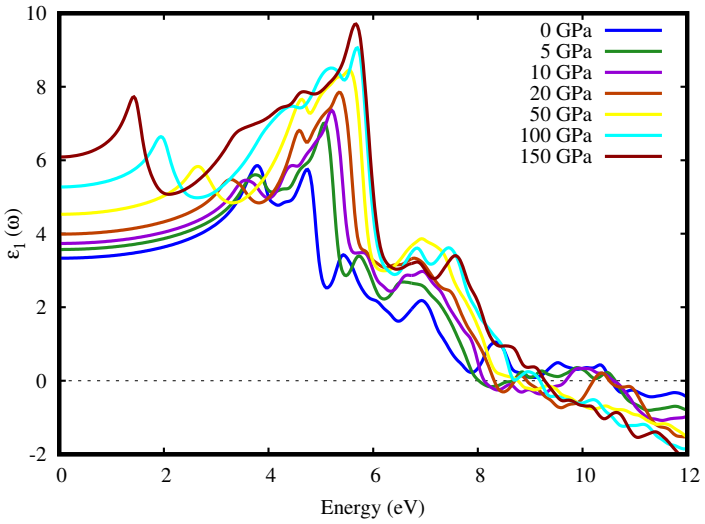

Figure 4.8: Calculated pressure-induced spectra of real portion of dielectric function of K_2YAgBr_6.

which provides useful knowledge about the charge carrier recombination rate and hence the entire potency of optoelectronic devices [97]. The materials which have improved value of dielectric function means the materials have low charge carrier recombination rate and greater efficiency of the optoelectronic devices. The real part expline the dispersion and degree of polarization of a compound as a response to the electromagnetic wave interactions whereas, the imaginary part indicates loss factor or absorption of light energy. Based on our calculation, at ambient pressure, the static dielectric function $\epsilon_1(\omega)$ is 3.4 eV which show that this material is good

dielectric can be used for designing of high-value capacitor. This value are consistent with high electron polarizability of this compound. The maximum polarizability oc-

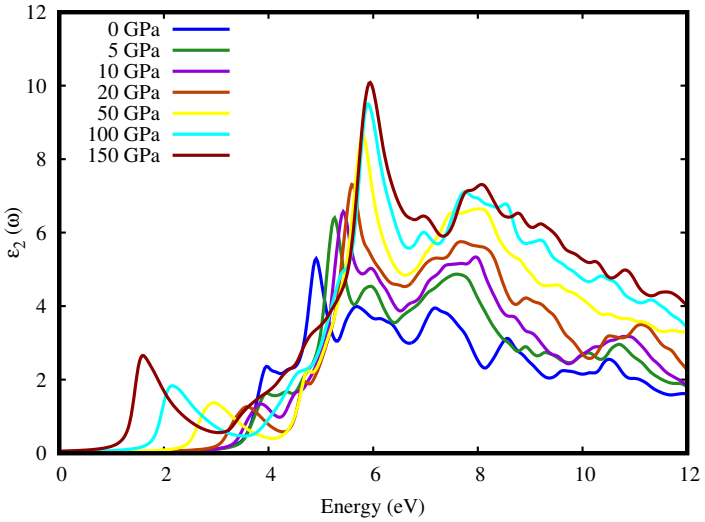

Figure 4.9: Calculated pressure-induced spectra of imaginary portion of dielectric function of K_2YAgBr_6.

curs inside the material when the polarization value rises from the static constant to the high peak [98]. As can be seen in the Figure 4.8 and 4.9 the most significant peak for both real and imaginary component of the function appear in the visible region. At 0 GPa, the static part of $\epsilon_1(\omega)$, express as $\epsilon_1(0)$, is 3.4. The static peak of dielectric function of both real and imaginary parts of K_2YAgBr_6 perovskite rises in the visible region with enhanced pressure. The further increase in incident photon energy enhances $\epsilon_1(\omega)$ to maxumum values $\epsilon_1(\omega)_{max} = 5.7$ at 0 GPa, the value of $\epsilon_1(\omega)_{max}$ gets increased with rise in the pressure and shifts toward higher energy due to decrease in band gap. Hence, $\epsilon_1(\omega)$ and $\epsilon_1(\omega)_{max}$ has inverse relation with band gap. For incident photon with the energy of $\hbar\omega > 4.9$ eV, $\epsilon_1(\omega)$ decreases with increasing of energy, as the plasmon frequency of the materil appears at the energy of $\hbar\omega = 10.2$ eV, at which $\epsilon_1(\omega) = 0$. As a result the real component turn into negetive value from this energy, so this materials exhibits metalic behavior from this energy, otherwise this material is semiconductor. The imaginary part of the dielectric function is associated directly with material band structure and explains its absorption nature [99]. $\epsilon_2(\omega)$ starts for each pressure at respective foundamental band gap. As, optical absorption take place for transition of charges from valanvce band maximum

(Br-4p states) to conduction minimum (Ag-4d states). In consequences of band gap decrease with pressure, the start of metarial optical effectiveness shifts from ultra-violet region to infrared region of electromagnetic spectrum. This makes K_2YAgBr_6 attractive for optical devices working in tunable ranges of electromagnetic radiation.

4.4.2 Absorption coefficient

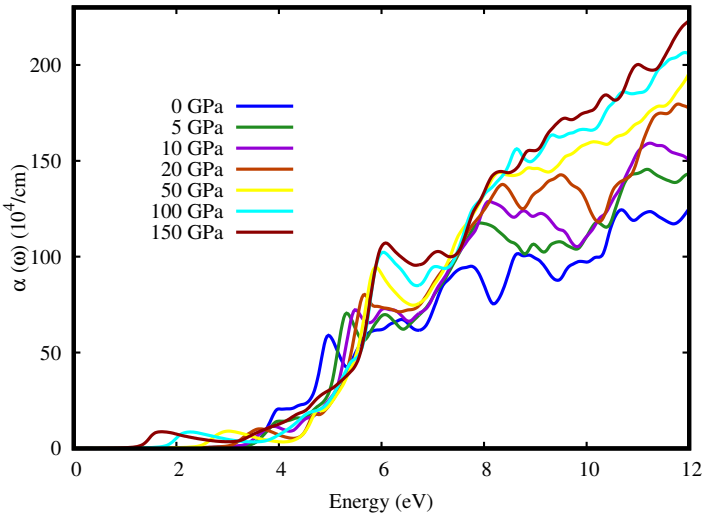

Figure 4.10: Calculated pressure-induced spectra of absorption coefficient of K_2YAgBr_6.

The optical absorption coefficient is a crucial to have knowledge about the capability of a material to absorb light energy and hence provides significant information about the solar energy conversion efficiency of the material which is required for the practical application of material in prominant performance solar cell and other photovoltaic devices [100]. The optical absorption coefficient is stated as the measurement of penetration of light at specific energy (wavelength) into the material before being absorbed. The analyzed optical absorption spectra of K_2YAgBr_6 perovskite as a function of photon energy under different hydrostatic pressures up to 150 GPa in Figure 4.10. The absorption edge of K_2YAgBr_6 shifts in the direction to the low energy region with increasing pressure that is consistent to the observation about pressure dependent band gap variation. As the band gap and the absorption edge vary within the visible region that shows complete transparency for the infrared energies. The calculated absorption coefficient shows non-linear increase due to the illustrated indirect band gap nature under hydrostatic pressure up to 150 GPa. The

maximum broad absorption peak lies in the ultraviolet region which indicates that the studied K_2YAgBr_6 double perovskite would be an efficient material to make devices to sterilize surgigal equipment. The maximum range of ultraviolet light enegry absorption of a material indicates its potential application surgical devices formation as sterilizing the devices made of such material becomes easier and efficient [101].

4.4.3 Optical conductivity

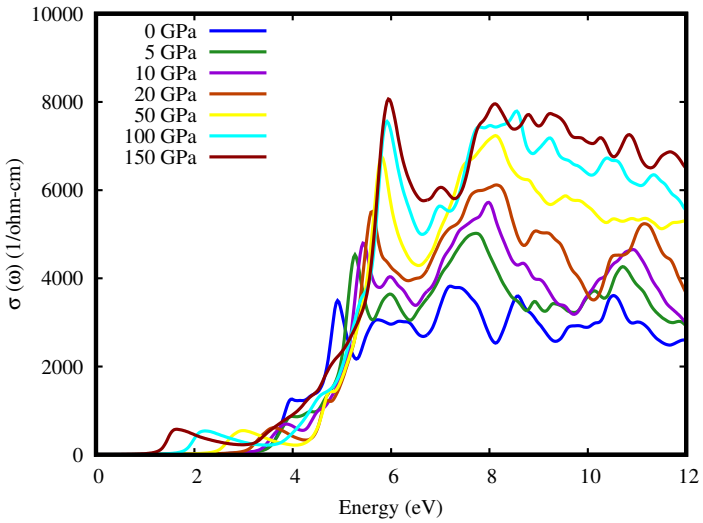

Figure 4.11: Calculated pressure-induced spectra of optical conductivity of K_2YAgBr_6.

The optical conductivity is basically another form of photoconductivity [102]. The $\sigma(\omega)$ value is the result of conduction of electrons when photon of a certain frequency falls on a material. The amount of photoconductivity as well as electrical conductivity enhances of increasing photons absorption. The conductivity spectra (real portion) under several hydrostatic pressures is illustrated in Figure 4.11 up to 12 eV of photon energy. At ambient pressure, the composition K_2YAgBr_6 starts conduction at 3.5 eV. The optical coductivity enhances with applied pressure which is a result of the enhancing absorption coefficient with increased pressure. The conductivity spectra has similar characteristics like absorption spectra shows in Figure 4.10 because, material releases free carriers for conduction when absorbs energy. The pressure-induced high energy shift of optical conductivity shows a potential in K_2YAgBr_6 for electrical device applications involving incident radiation.

4.4.4 Reflectivity

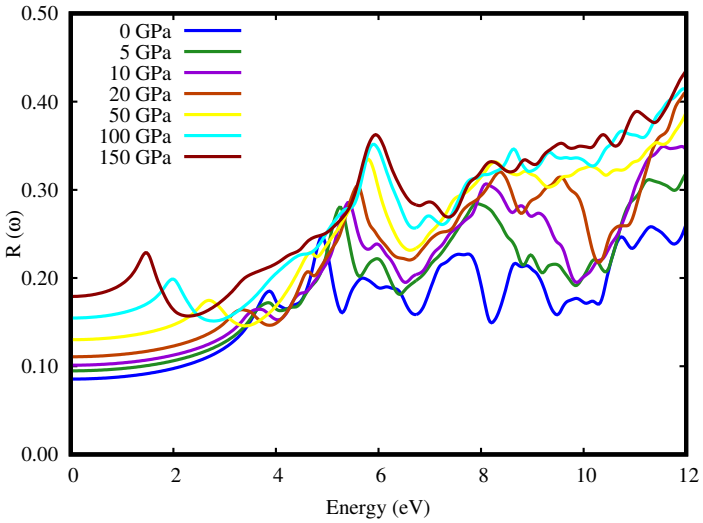

Figure 4.12: Calculated pressure-induced spectra of reflectivity of K_2YAgBr_6.

The surface nature of the K_2YAgBr_6 perovskite can be understood in terms of reflected light energy from the surface [100]. The reflactivity R(ω) spectra as a function of electromagnetic radiation was calculated with various pressures as shown in Figure 4.12 . The static value of Reflectivity R(0) was computed as 0.07, which increase with pressure as tabulated in Table 4.2. The peak value of reflectivity was obtained within energy range of 5eV - 7 eV. In this energy range K_2YAgBr_6 reflects all incident radiations. The variation of peaks in intensity is due to the reflection of light photons at different angles of the material surface. The amount of reflectivity increases as much as enhanced pressure which may cause to reduce the potency of the solar cell.

4.4.5 Refractive index

The light scattering fraction was evaluated by calculating the refractive index throught the material. The refractive index and static dielectric function are related by the equation $n^2(0) = \epsilon_1(0)$. Therefore, this explain the energy dependence changed from n^2 to $\epsilon_1(0)$ as shown in Table 4.2. The spectrum of refractive index n(ω) for K_2YAgBr_6 was calculated and shown in figure 4.13. The trend of n(ω) is similar as $\epsilon_1(\omega)$. Its values starts with a static value n(0) of 1.8 at ambient pressure and

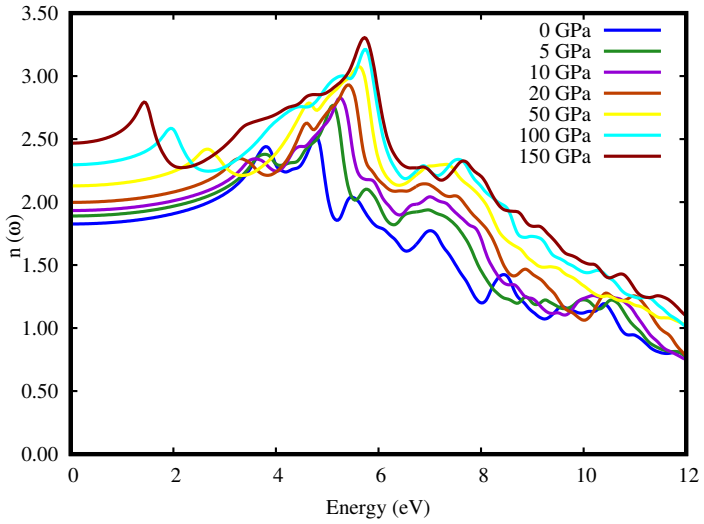

Figure 4.13: Calculated pressure-induced spectra of refractive index of K_2YAgBr_6.

reaches to a maximum $n(\omega)_{max} = 2.5$ at 4.5 eV energy. With increases in pressure the $n(\omega)_{max}$ also increases and shifts to higher energies. After 10.8 eV, the value of n(ω) decreases below unity. In this region the group velocity ($V_g = \frac{c}{n}$) of incident radiations is greater than c because refractive index has value less than unity [103,104]. The fractinal V_g elucidate the materials showing group velocity enhances than the velocity of light illustrating superluminal nature that show photonic application.

4.5 Thermoelectric properties

To shorten environmental pollution and to avoid energy disasters, thermoelectric materials are of great interest, transforming wasted heat into useful electricity [105–107]. As it has been exploited in various applications in our daily life like thermoelectric refrigeration, computer cooling and especially in solar cells [108,109]. To manufacture all these devices we must choose materials with thermoelectric properties at room temperature (300 K). The figure of merit (ZT) is usually used to mention the inclusive thermoelectric quality of a material. We can be calculated the value of figure of merit in terms of electrical conductivity ($\frac{\sigma}{\tau}$), Seebeck coefficient

(S) and thermal conductivity ($\frac{k}{\tau}$)using the equation:

$$ZT = \frac{S^2 \times \sigma}{(k_e \times k_L)} \tag{4.4}$$

Thermoelectric behavior calculating by BoltzTrap program [110], which depends on a well-tested smoothed Fourier interpolation to obtain an analytical expression of bands. Heat conduction is primarily mediated by the free electrons devices, therefore, it could utilized by employing efficient thermoelectric materials.

4.5.1 Electrical conductivity

Electrical conductivity is a measure of material's ability to conduct electric current. It quantifies how easily electrons (or other charge carriers) can move through the material when an electric field is applied conduction in materials induced due to carriers free motion from one point to another point. There are two different factor for conductivity in semiconductor materials such as carrier concentrations and the carrier mobilities. These can be written in mathematical form, $\sigma = n_e\mu_e + n_h\mu_h$. The electrical conductivity of a material can be used to quantify the flow of charge through it. The calculated electrical conductivity by relaxation time (σ/τ) as a function of tempareture was ploted in Figure 4.14 between temperature range 100 - 1000 K. At ambient pressure electrical conductivity is $0.9 \times 10^{19}(\Omega.m.s)^{-1}$ at 300K, which

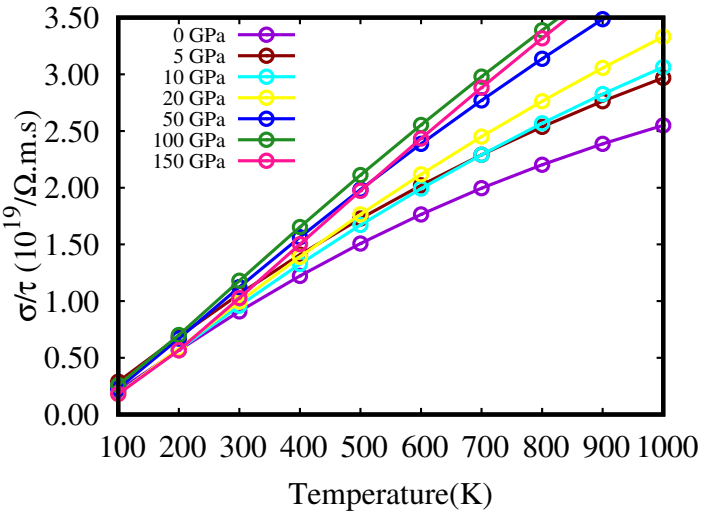

Figure 4.14: Calculated electrical conductivity under different hydrostatic pressure.

linearly improves with the rising in temperature and attains $2.3 \times 10^{19}(\Omega.m.s)^{-1}$ at 800K. when we applied pressure up to 150 GPa, this conductivity gradually increase with temperature reaching a maximum value of $3.4 \times 10^{19}(\Omega.m.s)^{-1}$ at 800K. Such increasing value of (σ/τ) at larger temperature is attributed to generation of more electrons (with large kinetic energies) due to bond breaking at elevated temperature. From literature, best thermoelectric substances e.g, PbTe, and Bi_2Te_3 demonstrate an increasing trend of electrical conductivity with temperature which is quite similar to our studied syestem. Therefore, we can speculate that computed material can be considered promising candidate for thermoelectric applications. The investigated compound semiconductor nature is supported by the increase in electrical conductivity, which represents a continually growing carrier concentration and implies a negative temperature coefficient of resistance.

4.5.2 Seebeck coefficient

The Seebeck coefficient S which determines the potential difference across temperature gradient ΔT between connection of two metals. Higher Seebeck coefficient values show that the large thermoelectric voltage is generated as the temperature rises that suggest practical device applications. Figure 4.15 shown the Seebeck coefficient for temperature range (100-1000) K measured from the expression S = ΔV/ΔT [111, 112]. The positive values of S for this composition reveal that positive charge carriers are the majority charge carriers in this material. At ambient pressure and 300 K temperature S found maximum about 217 μV/K for K_2YAgBr_6 compound while with increasing temperature S linearly decreased, observed 214 μV/K for K_2YAgBr_6 compound at 800 K temperature as shown in the figure. We also investigated the Seebeck coefficient against temperature for K_2YAgBr_6 double perovskite under different pressures upto 150 GPa as shown in Figure 4.15. we see that Seebeck coefficient decreased with rising temperature and also decreased under pressure. To be more precise, at room temperature (300 K), the seebeck coefficient reaches 214 μV/K to 240 μV/K when we applied pressure (0 - 150) GPa respectively which are higher than 202 μV/K which is the optimum value of Seebeck coefficient for a good thermoelectric material posed by Hong, et al. [113]. Under all applied

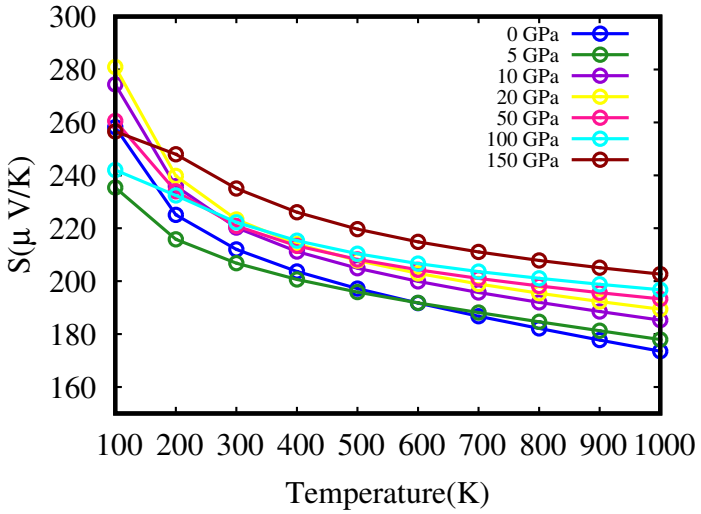

Figure 4.15: Calculated seebeck coefficient under different hydrostatic pressure.

pressure, the value of S gradually increases compared to 0 GPa for K_2YAgBr_6 double perovskite. Thus, the studied double perovskite material under hydrostatic pressure are excillent for thermoelectric application.

4.5.3 Thermal conductivity

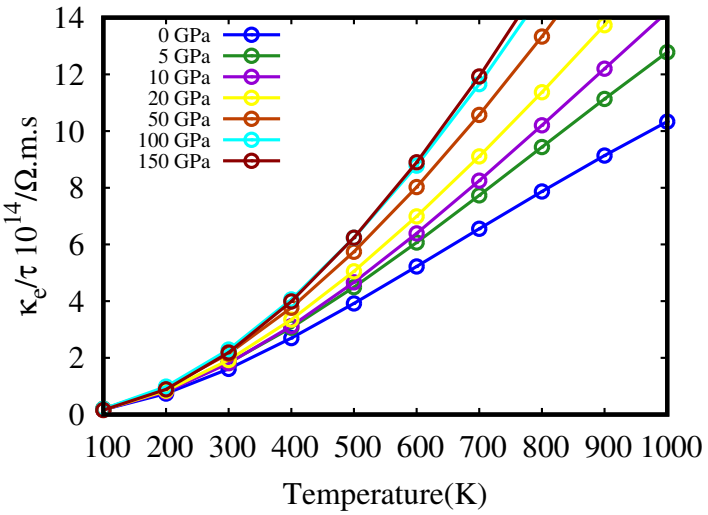

Figure 4.16: Calculated thermal conductivity under different hydrostatic pressure.

The lattice vibration created in the materials through the conduct of thermally excited electrons which effect in the total thermal conductivity $(\kappa_e)/\tau)$ having electronic and phonons parts that can be expressed as $k = \kappa_e + \kappa_{ph}$. The electronic part of the thermal conductivity, (κ_e), has also been calculated for K_2YAgBr_6 and is pre-

sented in Figure 4.16. The participation of phonons can be neglected at minimum temperature [114]. At 0 GPa the thermal conductivity, (κ_e/τ), exhibit smaller values in the low temperature range; however, it reaches to 1.710^{14} $(\Omega.m.s)^{-1}$ at 300 K and attains maximum value of 810^{14} $(\Omega.m.s)^{-1}$ at 800 K. The increase in the value of (κ_e/τ) with temperature indicates that at a higher temperature more lattice vibrations are generated, which causes an increase in (κ_e/τ) [115]. So for the best thermoelectric materials should be the thermal to electrical conductivity $(\frac{\kappa_e}{\sigma})$ very small, therefore, this ratio being of the order of 10^6 suggests the studied compound as appropriate thermoelectric material [116].

4.5.4 Power factor

The power factor (PF) is another thermoelectric parameter that is used to determine the thermoelectric performance of any materials and this is calculated by the expression PF = $S^2\sigma$. The temperature dependent variation of PF is shown in Figure 4.17. The efficiency of this thermoelectric material without including (κ_e/τ) can be explained using power factor ($S2\sigma$) should be considerably high. The indirect band gap K_2YAgBr_6 (at 0 GPa) increases from zero and becomes maximum 4 W/mK^2S at 300 K and then continously increases to 7.8 W/mK^2S with further increasing temperature up to 800 K. We also investigated power factor against temperature

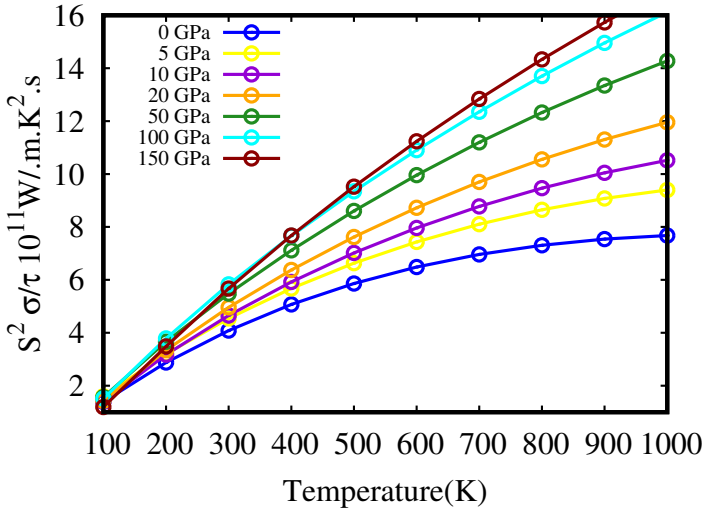

Figure 4.17: Calculated power factor under different hydrostatic pressure.

under hydrostatic pressure for compounds as shown in Figure 4.17. After applying pressure, the power factor increases gradually for with increase temperature.

4.5.5 Figure of merits

Most important among the thermoelectric parameters is the figure of merit (ZT). It determines the efficacy of thermoelectric devices and is calculated using the expression ZT = $S^2\sigma$ T κ, where S, σ, κ and T represent the Seebeck coefficient, electrical conductivity, thermal conductivity and temperature in kelvin respectively [109]. The variation of ZT for K_2YAgBr_6 double perovskite in the temperature range $100 - 1000$ K under hydrostatic pressure is shown in Figure 4.18. At ambient pressure, the maximum value of ZT is 0.71 at room temperature (300 K). At ambient pressure, it is about 0.71 at room temperature (300K) which increases with an increase of temperature and become 0.8 at 1000K temperature. However, the room temperature values of ZT and electronic thermoelectric parameter under pressure are presented in the plot. When we applied pressure up to 150 GPa, ZT increases with temperature for all pressure. These observations indicate that the compositions under study have potential for use in thermoelectric applications [117]. The large values of electrical conductivities and Seebeck coefficients and values of ZT close to unity make these materials very attractive for thermoelectric device applications.

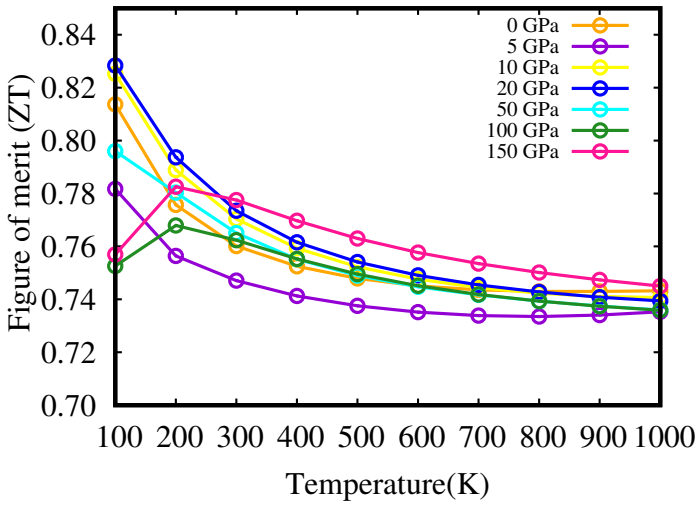

Figure 4.18: Calculated figure of merits under different hydrostatic pressure.

4.6 Mechanical properties

The elastic constants of solid materials are crucial parameters as they provide significant link between the mechanical properties and fruitful information concerning the characteristic of existing forces in solids and particularly for the material stability and stiffness [118, 119]. Elastic constants also provide dynamic information about the ability of a crystal to resist external pressure. As lattice parameter reduces with pressure, it is very significant to investigate the influences of pressure on the elastic constants for the purpose of understanding the mechanical properties of K_2YagBr_6 double perovskite. Cubic structure crystals like pressure-induced K_2YAgBr_6 have three indipendent elastic moduli C_{ij}, these are C_{11}, C_{12}, and C_{44}. The simulated elastic parameters under variant pressures with available other theoritical result are listed in Table 4.2. The mechanical stability of a crystal can be satisfied with its elastic constants using Born crireria which is expressed as: $C_{11} - C_{12} > 0$, $C_{11} > 0$, $C_{44} > 0$, $C_{11} + 2C_{12} > 0$, $C_{12} < B < C_{11}$ Table 4.2 shows that the K_2YAgBr_6 double perovskite is mechanically stable under cosiderable varient pressure as satisfies the above stability criteria. Moreover, the present computed values of elastic constants and other mechanical properties at zero pressure are very well matched with previous available DFT result [91], bearing nicety of the present calculation. From table 4.2, it can be observed that the values of C_{11} and C_{12} and C_{44} increase rapidly with pressure going up to 150 GPa. The elastic constants C_{11} and $C_{12}$are connected with the elasticity in length, increase with pressure enhanced [120]. Whereas, C_{44} is connected with the elasticity in shape, which provides relation between the deformation in shape and the stiffness [120]. The Cauchy pressure (C_{12} - C_{44}) is well-known parameter to indicate te ductile and brittle characteristics of materials. The negetive value of Cauchy pressure of a material indicates its brittle and positive value of Cauchy pressure of a material indicates its ductile nature. It can be seen that the Cauchy pressure value of K_2YAgBr_6 double perovskite under all studied is positive as zero pressure and increases with pressure enhanced, which indicates the ductile nature of the perovskite increases with pressure enhanced.

The mechanical properties such as Bulk modulus (B), Shear modulus (G), Young's

Table 4.2: Calculated elastic constant C_{11}, C_{12}, C_{44}, Cauchy's pressure of K_2YAgBr_6 under hydrostatic pressure.

Pressures (GPa)	C_{11}	C_{12}	C_{44}	$C_{12} - C_{44}$
0	22.42	19.89	5.81	14.07
5	77.42	29.58	6.22	23.36
10	109.96	31.51	8.24	23.27
20	166.36	40.27	7.09	33.17
50	289.98	63.08	3.30	59.78
100	424.81	93.72	0.09	93.63
150	545.50	113.61	-3.50	117.11

modulus (Y), Pugh's ratio (B/G), and Poisson's ratio (ν) of the cubic K_2YAgBr_6 double perovskite are calculated with help of well-known expressions as given in literature [100] and listed in Table 4.3. The lower values of B, G and Y of the K_2YAgBr_6 double perovskite under zero pressure indicates it's as soft material. It can be noticed that the values of B, G,and Y rises with increased pressure, which indicates the applying hydrostatic pressure provides benefit to the hardness of K_2YAgBr_6. Ying et al. [121] also showed that the values of elastic moduli of K_2YAgBr_6 increase with enhanced pressure. The bulk and shear moduli that can forecast the hardness of material can be found using the Viogt-Reuss-Hill averaging scheme approach [122]. The Viogt limits of the bulk modulus (B) and shear modulus (G) for the cubic system are as follows:

$$B_v = \frac{(C_{11} + 2C_{12})}{3} \tag{4.5}$$

$$G_v = \frac{(C_{11} - C_{12} + 3C_{44})}{5} \tag{4.6}$$

However, the Reuss formulae for the bulk and shear moduli are:

$$B_v = B_R \tag{4.7}$$

Table 4.3: The calculated the Bulk modulus B (GPa), the Shear modulus G (GPa), Young's modulus Y (GPa), the elastic anisotropy factor (A), B/G ratio and Poisson's ratio (ν) of K_2YAgBr_6 under hydrostatic pressure.

Pressures (GPa)	B	G	Y	A	B/G	ν
0	20.73	3.19	9.10	4.59	6.50	0.42
5	45.52	11.60	30.71	0.26	4.11	0.38
10	57.66	16.34	44.78	0.21	3.52	0.37
20	82.30	20.24	56.11	0.11	4.06	0.38
50	138.71	26.37	74.41	0.02	5.25	0.41
100	204.08	37.48	105.92	0.00	5.44	0.40
150	257.58	39.18	111.89	-0.01	6.57	0.42

$$G_R = \frac{5(C_{11} - C_{12}C_{44})}{4C_{44} + 3(C_{11} - C_{12})} \tag{4.8}$$

Using Hill's average approximation the bulk and shear moduli are defined as;

$$B = \frac{B_v + B_R}{2} \tag{4.9}$$

$$G = \frac{G_v + G_R}{2} \tag{4.10}$$

Young's modulus, determines the strength of material is ratio of linear stress and strain can be evaluated via relation.

$$Y = \frac{9BG}{3B + G} \tag{4.11}$$

The Pugh's ratio is an important factor to indicate ductile and brittle behavior of a crystal. The low value of B/G indicates the brittle and high value of B/G indicates the ductile nature of the material and the critical value is considered as 1.75 [123]. Table 4.43 shows that the B/G value of K_2YAgBr_6 double perovskite under zero pressure is greater than the the critical value which reveals the ductile nature of

the material. It is also noticed that the B/G value increases with the increase of pressure, which indicates that the ductility of K_2YAgBr_6 can be improved by the rise of pressure.

The Poisson's ratio ν is very useful criteria which provides fruitful knowledge about the bonding forces and stability of a crystal. The maximum value and minimum value of ν for existing central forces in ionic crystals are cosidered as 0.5 and 0.25 respectively [124]. Ionic crystal's interatomic forces are central forces. From Table 4.3, it can be noticed that the value of ν of K_2YAgBr_6 double perovskite at ambient condition is 0.42 which is lower than 0.5 but greater than 0.25, indicating the existence of central forces in the K_2YAgBr_6 double perovskite. The value of ν increases with increasing pressure.

The (ν) is also a useful indicator of brittleness and ductility of materials. The critical value of ν to indicate ductile and brittle behavior of material is 0.26 [100]. The value of ν of K_2YAgBr_6 double perovskite without any external pressure is higher than 0.26 as displayed in Table 4.3, which reveals the ductile characteristics of the perovskite. The value of ν increases with the increase of pressure, which predicts that the ductility can be improved further by applying external pressure. The variation of B/G and ν of K_2YAgBr_6 with pressure , it is evident that the ductility of K_2YAgBr_6 increases with enhanced pressure and hence pressure can be an efficient approach where high ductility is required to fabricate devices of K_2YAgBr_6.

Chapter 5

Conclusions

In brief the structural, elastic, optoelectronic, and thermoelectric properties of K_2YAgBr_6 double perovskite under hydrostatic pressure have been studied using DFT calculations. The lattice constant and cell volume of the K_2YAgBr_6 decreases with pressure. The elastic moduli increases with pressure, which benefits to the hardness of K_2YAgBr_6. The study of Poissins's ratio and Pugh's shows that the K_2YAgBr_6 material has increasing affinity of ductility with increasing pressure and the material can be efficient for practical devices application where high ductility is needed. The band gap decreases with pressure and shows indirect band gap for all pressure range. The optical absorption as well as conductivity increase remarkably in the ultraviolet region with enhanced pressure. The visible region of absorption is worthy for photovoltaic domain and the ultraviolate region is more suitable for optoelectronic devices such as UV Photodetectors, Light-Emitting Diodes and Photovoltaic devices can be improved greatly by inducing pressure. After increasing pressure reduces the bandgap, enhances electrical conductivity, and thermal conductivity. This tunability under pressure make this material more efficient in converting heat into electricity. The structural stablity, the calculated indirect band gap, optical properties and thermoelectric properties make them possible to use this double perovskite K_2YAgBr_6 in different optoelectronic and thermoelectric applications.

Bibliography

[1] Shafiqur Rehman, Luai M Alhems, Md Mahbub Alam, Longjun Wang, and Zakria Toor. A review of energy extraction from wind and ocean: Technologies, merits, efficiencies, and cost. *Ocean Engineering*, 267:113192, 2023.

[2] Mohammed Ismael. Ferrites as solar photocatalytic materials and their activities in solar energy conversion and environmental protection: a review. *Solar Energy Materials and Solar Cells*, 219:110786, 2021.

[3] Hanbee Lee, Zhi Jiang, Tomoyuki Yokota, Kenjiro Fukuda, Sungjun Park, and Takao Someya. Stretchable organic optoelectronic devices: Design of materials, structures, and applications. *Materials Science and Engineering: R: Reports*, 146:100631, 2021.

[4] Huanping Zhou, Qi Chen, Gang Li, Song Luo, Tze-bing Song, Hsin-Sheng Duan, Ziruo Hong, Jingbi You, Yongsheng Liu, and Yang Yang. Interface engineering of highly efficient perovskite solar cells. *Science*, 345:542–546, 2014.

[5] Julian Burschka, Norman Pellet, Soo-Jin Moon, Robin Humphry-Baker, Peng Gao, Mohammad K Nazeeruddin, and Michael Grätzel. Sequential deposition as a route to high-performance perovskite-sensitized solar cells. *Nature*, 499:316–319, 2013.

[6] Erjin Zheng, Brian Yuh, Gabriella A Tosado, and Qiuming Yu. Solution-processed visible-blind uv-a photodetectors based on $CH_3NH_3PbCl_3$ perovskite thin films. *Journal of Materials Chemistry C*, 5:3796–3806, 2017.

[7] Andrew Barnabas Wong, Minliang Lai, Samuel Wilson Eaton, Yi Yu, Elbert Lin, Letian Dou, Anthony Fu, and Peidong Yang. Growth and anion exchange

conversion of CH_3NHPbX_3 nanorod arrays for light-emitting diodes. *Nano Letters*, 15:5519–5524, 2015.

[8] Christopher Eames, Jarvist M. Frost, Piers R.F. Barnes, Brian C. O'regan, Aron Walsh, and M. Saiful Islam. Ionic transport in hybrid lead iodide perovskite solar cells. *Nature Communications*, 6:7497, 2015.

[9] Xinjiang Wang, Tianshu Li, Bangyu Xing, Muhammad Faizan, Koushik Biswas, and Lijun Zhang. Metal halide semiconductors beyond lead-based perovskites for promising optoelectronic applications. *The Journal of Physical Chemistry Letters*, 12:10532–10550, 2021.

[10] Gongxi Qiao, Zhi Zeng, Jinwei Gao, Yiping Tang, and Qianming Wang. An efficient route to assemble novel organometal halide perovskites and emission evolution performance. *Journal of Alloys and Compounds*, 771:418–423, 2019.

[11] Xingyu Liu, Jinwei Gao, Wanqiang Liu, and Qianming Wang. Reinforcing effects of waterproof substrate on the photo-, thermal and pH stabilities of perovskite nanocrystals. *Journal of Alloys and Compounds*, 817:152693, 2020.

[12] Xingyu Liu, Jinwei Gao, and Qianming Wang. Structural-property correlations of all-inorganic $CsPbBr_3$ perovskites via synergetic controls by $PbBr_2$, 2-mercapto-3-methyl-4-thiazoleacetic acid and water. *Chemical Engineering Journal*, 428:131117, 2022.

[13] Takumi Yamada, Yasuhiro Yamada, and Yoshihiko Kanemitsu. Photon recycling in perovskite $CH_3NH_3PbX_3$(X= I, Br, Cl) bulk single crystals and polycrystalline films. *Journal of Luminescence*, 220:116987, 2020.

[14] Rui He, Shengqiang Ren, Cong Chen, Zongjin Yi, Yi Luo, Huagui Lai, Wenwu Wang, Guanggen Zeng, Xia Hao, Ye Wang, et al. Wide-bandgap organic–inorganic hybrid and all-inorganic perovskite solar cells and their application in all-perovskite tandem solar cells. *Energy Environmental Science*, 14:5723–5759, 2021.

[15] Sanjay Pachori, Rohit Agarwal, Akash Shukla, Upasana Rani, and Ajay Singh Verma. Mechanically stable with highly absorptive formamidinium lead halide perovskites [$(HC(NH_2)_2PbX_3$; X= Br, Cl]: Recent advances and perspectives. *International Journal of Quantum Chemistry*, 121:e26671, 2021.

[16] Lucia Fagiolari and Federico Bella. Carbon-based materials for stable, cheaper and large-scale processable perovskite solar cells. *Energy Environmental Science*, 12:3437–3472, 2019.

[17] Kyle Frohna, Tejas Deshpande, John Harter, Wei Peng, Bradford A Barker, Jeffrey B Neaton, Steven G Louie, Osman M Bakr, David Hsieh, and Marco Bernardi. Inversion symmetry and bulk rashba effect in methylammonium lead iodide perovskite single crystals. *Nature Communications*, 9:1829, 2018.

[18] Giacomo Giorgi, Jun-Ichi Fujisawa, Hiroshi Segawa, and Koichi Yamashita. Small photocarrier effective masses featuring ambipolar transport in methylammonium lead iodide perovskite: a density functional analysis. *The Journal of Physical Chemistry Letters*, 4:4213–4216, 2013.

[19] Anees A Ansari, MK Nazeeruddin, and Mohammad Mahdi Tavakoli. Organic-inorganic upconversion nanoparticles hybrid in dye-sensitized solar cells. *Coordination Chemistry Reviews*, 436:213805, 2021.

[20] Naveen Kumar, Jyoti Rani, and Rajnish Kurchania. Advancement in $CsPbBr_3$ inorganic perovskite solar cells: Fabrication, efficiency and stability. *Solar Energy*, 221:197–205, 2021.

[21] Tianhao Wu, Xiao Liu, Xinhui Luo, Xuesong Lin, Danyu Cui, Yanbo Wang, Hiroshi Segawa, Yiqiang Zhang, and Liyuan Han. Lead-free tin perovskite solar cells. *Joule*, 5:863–886, 2021.

[22] Hongwei Lei, David Hardy, and Feng Gao. Lead-free double perovskite $Cs_2AgBiBr_6$: fundamentals, applications, and perspectives. *Advanced Functional Materials*, 31:2105898, 2021.

[23] Femi Igbari, Zhao-Kui Wang, and Liang-Sheng Liao. Progress of lead-free halide double perovskites. *Advanced Energy Materials*, 9:1803150, 2019.

[24] Wan-Jian Yin, Baicheng Weng, Jie Ge, Qingde Sun, Zhenzhu Li, and Yanfa Yan. Oxide perovskites, double perovskites and derivatives for electrocatalysis, photocatalysis, and photovoltaics. *Energy Environmental Science*, 12:442–462, 2019.

[25] Zewen Xiao, Zhaoning Song, and Yanfa Yan. From lead halide perovskites to lead-free metal halide perovskites and perovskite derivatives. *Advanced Materials*, 31:1803792, 2019.

[26] Sasha Khalfin and Yehonadav Bekenstein. Advances in lead-free double perovskite nanocrystals, engineering band-gaps and enhancing stability through composition tunability. *Nanoscale*, 11:8665–8679, 2019.

[27] Mehri Ghasemi, Mengmeng Hao, Mu Xiao, Peng Chen, Dongxu He, Yurou Zhang, Weijian Chen, Jiandong Fan, Jung H Yun, Baohua Jia, et al. Lead-free metal-halide double perovskites: from optoelectronic properties to applications. *Nanophotonics*, 10:2181–2219, 2020.

[28] Liang Chu, Waqar Ahmad, Wei Liu, Jian Yang, Rui Zhang, Yan Sun, Jianping Yang, and Xing'ao Li. Lead-free halide double perovskite materials: a new superstar toward green and stable optoelectronic applications. *Nano-Micro Letters*, 11:1–18, 2019.

[29] Adam H Slavney, Te Hu, Aaron M Lindenberg, and Hemamala I Karunadasa. A bismuth-halide double perovskite with long carrier recombination lifetime for photovoltaic applications. *Journal of the American Chemical Society*, 138:2138–2141, 2016.

[30] M Tariq, Malak Azmat Ali, A Laref, and G Murtaza. Anion replacement effect on the physical properties of metal halide double perovskites Cs_2AgInX_6(X= F, Cl, Br, I). *Solid State Communications*, 314:113929, 2020.

[31] Xiaoqing Yang, Huimin Xiang, Jianying Huang, Chuan Zhou, Ran Ran, Wei Wang, Wei Zhou, and Zongping Shao. Thiourea with sulfur-donor as an effective additive for enhanced performance of lead-free double perovskite photovoltaic cells. *Journal of Colloid and Interface Science*, 628:476–485, 2022.

[32] Dolly Kumari and Saurabh Kumar Pandey. Comprehensive study and performance analysis of an eco-friendly double perovskite $Cs_2AgBiBr_6$ on Si tandem solar cell. *JOSA B*, 39:756–763, 2022.

[33] Xiaoqing Yang, Yonghui Chen, Pengyun Liu, Huimin Xiang, Wei Wang, Ran Ran, Wei Zhou, and Zongping Shao. Simultaneous power conversion efficiency and stability enhancement of $Cs_2AgBiBr_6$ lead-free inorganic perovskite solar cell through adopting a multifunctional dye interlayer. *Advanced Functional Materials*, 30:2001557, 2020.

[34] Xiaoqing Yang, Wei Wang, Ran Ran, Wei Zhou, and Zongping Shao. Recent advances in $Cs_2AgBiBr_6$-based halide double perovskites as lead-free and inor-

ganic light absorbers for perovskite solar cells. *Energy Fuels*, 34:10513–10528, 2020.

[35] Jiban Kangsabanik, Vipinraj Sugathan, Anuradha Yadav, Aswani Yella, and Aftab Alam. Double perovskites overtaking the single perovskites: A set of new solar harvesting materials with much higher stability and efficiency. *Physical Review Materials*, 2:055401, 2018.

[36] Eric T McClure, Molly R Ball, Wolfgang Windl, and Patrick M Woodward. Cs_2AgBiX_6 (X= Br, Cl): new visible light absorbing, lead-free halide perovskite semiconductors. *Chemistry of Materials*, 28:1348–1354, 2016.

[37] Tian Wang, Dongting Yue, Xin Li, and Yixin Zhao. Lead-free double perovskite $Cs_2AgBiBr_6$/RGO composite for efficient visible light photocatalytic H_2 evolution. *Applied Catalysis B: Environmental*, 268:118399, 2020.

[38] Ghulam M Mustafa, Abdul Slam, Sadaf Saba, NA Noor, M Waqas Iqbal, and A Dahshan. Optoelectronic and thermoelectric characteristics of halide based double perovskites K_2YAgX_6 (X= Br, I) for energy storage applications. *Polyhedron*, 229:116184, 2023.

[39] Lingrui Wang, Kai Wang, and Bo Zou. Pressure-induced structural and optical properties of organometal halide perovskite-based formamidinium lead bromide. *The Journal of Physical Chemistry Letters*, 7:2556–2562, 2016.

[40] Yonggang Wang, Xujie Lu, Wenge Yang, Ting Wen, Liuxiang Yang, Xiangting Ren, Lin Wang, Zheshuai Lin, and Yusheng Zhao. Pressure-induced phase transformation, reversible amorphization, and anomalous visible light response in organolead bromide perovskite. *Journal of the American Chemical Society*, 137:11144–11149, 2015.

[41] Guan Yuan, Shan Qin, Xiang Wu, Hongrui Ding, and Anhuai Lu. Pressure-induced phase transformation of $CsPbI_3$ by x-ray diffraction and raman spectroscopy. *Phase Transitions*, 91:38–47, 2018.

[42] Diwen Liu, Qiaohong Li, Huijuan Jing, and Kechen Wu. Pressure-induced effects in the inorganic halide perovskite $CsGeI_3$. *RSC Advances*, 9:3279–3284, 2019.

[43] Yang Huang, Lingrui Wang, Zhuang Ma, and Fei Wang. Pressure-induced band structure evolution of halide perovskites: a first-principles atomic and

electronic structure study. *The Journal of Physical Chemistry C*, 123:739–745, 2018.

[44] IP Swainson, MG Tucker, DJ Wilson, B Winkler, and V Milman. Pressure response of an organic- inorganic perovskite: methylammonium lead bromide. *Chemistry of Materials*, 19:2401–2405, 2007.

[45] MA Ghebouli, T Chihi, B Ghebouli, and M Fatmi. Study of the structural, elastic, electronic and optical properties of lead free halide double perovskites Cs_2AgBiX_6(X= Br, Cl). *Chinese Journal of Physics*, 56:323–330, 2018.

[46] Eric Yang and Xuan Luo. Theoretical pressure-tuning bandgaps of double perovskites $A_2(BB')X_6$ for photo-voltaics. *Solar Energy*, 207:165–172, 2020.

[47] Yongfu Liang, Xiaoli Huang, Yanping Huang, Xin Wang, Fangfei Li, Youchun Wang, Fubo Tian, Bingbing Liu, Ze Xiang Shen, and Tian Cui. New metallic ordered phase of perovskite $CsPbI_3$ under pressure. *Advanced Science*, 6:1900399, 2019.

[48] Tingting Yin, Bo Liu, Jiaxu Yan, Yanan Fang, Minghua Chen, Wee Kiang Chong, Shaojie Jiang, Jer-Lai Kuo, Jiye Fang, Pei Liang, et al. Pressure-engineered structural and optical properties of two-dimensional $(C_4H_9NH_3)_2PbI_4$ perovskite exfoliated nm-thin flakes. *Journal of the American Chemical Society*, 141:1235–1241, 2018.

[49] Zhiwei Ma, Zhun Liu, Siyu Lu, Lingrui Wang, Xiaolei Feng, Dongwen Yang, Kai Wang, Guanjun Xiao, Lijun Zhang, Simon AT Redfern, et al. Pressure-induced emission of cesium lead halide perovskite nanocrystals. *Nature Communications*, 9:4506, 2018.

[50] Nazila Zarabinia and Reza Rasuli. Electronic and optical properties of halide double-perovskites under strain: A density functional study. *Energy Sources, Part A: Recovery, Utilization, and Environmental Effects*, 43:2443–2455, 2021.

[51] Ling-yi Huang and Walter RL Lambrecht. Electronic band structure, phonons, and exciton binding energies of halide perovskites $CsSnCl_3$, $CsSnBr_3$, and $CsSnI_3$. *Physical Review B—Condensed Matter and Materials Physics*, 88:165203, 2013.

[52] Karlheinz Schwarz and Peter Blaha. Solid state calculations using WIEN2k. *Computational Materials Science*, 28:259–273, 2003.

[53] Erwin Schrödinger. An undulatory theory of the mechanics of atoms and molecules. *Physical Review*, 28:1049, 1926.

[54] Robert G Parr and Weitao Yang. Density-functional theory of the electronic structure of molecules. *Annual Review of Physical Chemistry*, 46:701–728, 1995.

[55] Walter Kohn. Nobel lecture: Electronic structure of matter wave functions and density functionals. *Reviews of Modern Physics*, 71:1253, 1999.

[56] David C Young. Density functional theory. *Computational Chemistry*, pages 42–48, 2001.

[57] Wolfgang Pauli. The connection between spin and statistics. *Physical Review*, 58:716, 1940.

[58] Arthur Jabs. Connecting spin and statistics in quantum mechanics. *Foundations of Physics*, 40(7):776–792, 2010.

[59] Jean-Michel Combes, Pierre Duclos, and Ruedi Seiler. The born-oppenheimer approximation. In *Rigorous Atomic and Molecular Physics*, pages 185–213. Springer, 1981.

[60] Michael P Marder. *Condensed matter physics*. John Wiley Sons, 2010.

[61] David J Griffiths and Darrell F Schroeter. *Introduction to quantum mechanics*. Cambridge university press, 2018.

[62] Hanno Essén. The physics of the born–oppenheimer approximation. *International Journal of Quantum Chemistry*, 12:721–735, 1977.

[63] Hubert Klar. The born-oppenheimer approximation revisited. *Journal of Applied Mathematics and Physics*, 8:1507–1514, 2020.

[64] F Schwabl. Quantum mechanics (QM I). ; Quantenmechanik (QM I). Eine Einfuehrung. 2007.

[65] Arthur Jabs. Connecting spin and statistics in quantum mechanics. *Foundations of Physics*, 40:776–792, 2010.

[66] Paul Adrien Maurice Dirac. A new notation for quantum mechanics. *Mathematical Proceedings of the Cambridge Philosophical Society*, 35:416–418, 1939.

[67] Wolfgang Pauli. The connection between spin and statistics. *Physical Review*, 58:716, 1940.

[68] Attila Szabo and Neil S Ostlund. *Modern quantum chemistry: introduction to advanced electronic structure theory*. Courier Corporation, 2012.

[69] Walter Kohn. Nobel lecture: Electronic structure of matter wave functions and density functionals. *Reviews of Modern Physics*, 71:1253, 1999.

[70] Robert G Parr and Weitao Yang. Density-functional theory of the electronic structure of molecules. *Annual review of physical chemistry*, 46:701–728, 1995.

[71] Pierre Hohenberg and Walter Kohn. Inhomogeneous electron gas. *Physical Review*, 136:B864, 1964.

[72] Paul W Ayers and Weitao Yang. Density functional theory. *Computational medicinal chemistry for drug discovery*, page 571, 2003.

[73] Axel D Becke. Density-functional exchange-energy approximation with correct asymptotic behavior. *Physical Review A*, 38:3098, 1988.

[74] John P Perdew, John A Chevary, Sy H Vosko, Koblar A Jackson, Mark R Pederson, Dig J Singh, and Carlos Fiolhais. Atoms, molecules, solids, and surfaces: Applications of the generalized gradient approximation for exchange and correlation. *Physical Review B*, 46:6671, 1992.

[75] John P Perdew, Kieron Burke, and Matthias Ernzerhof. Generalized gradient approximation made simple. *Physical Review Letters*, 77:3865, 1996.

[76] Vladimir I Anisimov, Ferdi Aryasetiawan, and AI Lichtenstein. First-principles calculations of the electronic structure and spectra of strongly correlated systems: the LDA+ U method. *Journal of Physics: Condensed Matter*, 9:767, 1997.

[77] MT Czyżyk and GA Sawatzky. Local-density functional and on-site correlations: The electronic structure of La_2CuO_4 and $LaCuO_3$. *Physical Review B*, 49:14211, 1994.

[78] Vlasdimir I Anisimov, IV Solovyev, MA Korotin, MT Czyżyk, and GA Sawatzky. Density-functional theory and NiO photoemission spectra. *Physical Review B*, 48:16929, 1993.

[79] Erik R Ylvisaker, Warren E Pickett, and Klaus Koepernik. Anisotropy and magnetism in the LSDA+ U method. *Physical Review B*, 79:035103, 2009.

[80] Stefan Grimme. Semiempirical gga-type density functional constructed with a long-range dispersion correction. *Journal of Computational Chemistry*, 27:1787–1799, 2006.

[81] Francis Birch. Finite elastic strain of cubic crystals. *Physical Review*, 71:809, 1947.

[82] Fabien Tran and Peter Blaha. Accurate band gaps of semiconductors and insulators with a semilocal exchange-correlation potential. *Physical Review Letters*, 102:226401, 2009.

[83] Peter Blaha, Karlheinz Schwarz, Georg KH Madsen, Dieter Kvasnicka, Joachim Luitz, et al. WIEN2k. *An Augmented Plane Wave+ Local Orbitals Program for Calculating Crystal Properties*, 60, 2001.

[84] Hendrik J Monkhorst and James D Pack. Special points for brillouin-zone integrations. *Physical Review B*, 13:5188, 1976.

[85] M Jamal, S Jalali Asadabadi, Iftikhar Ahmad, and HA Rahnamaye Aliabad. Elastic constants of cubic crystals. *Computational Materials Science*, 95:592–599, 2014.

[86] Georg KH Madsen and David J Singh. BoltzTraP. A code for calculating band-structure dependent quantities. *Computer Physics Communications*, 175:67–71, 2006.

[87] Showkat H Mir, Prakash C Jha, Muhammed Shafiqul Islam, Amitava Banerjee, Wei Luo, Shweta D Dabhi, Prafulla K Jha, and Rajeev Ahuja. Static and dynamical properties of heavy actinide monopnictides of lutetium. *Scientific Reports*, 6:29309, 2016.

[88] Alexander E Fedorovskiy, Nikita A Drigo, and Mohammad Khaja Nazeeruddin. The role of goldschmidt's tolerance factor in the formation of $A_2BB'X_6$ double halide perovskites and its optimal range. *Small Methods*, 4:1900426, 2020.

[89] Chonghe Li, Kitty Chi Kwan Soh, and Ping Wu. Formability of ABO_3 perovskites. *Journal of Alloys and Compounds*, 372:40–48, 2004.

[90] Chonghea Li, Xionggang Lu, Weizhong Ding, Liming Feng, Yonghui Gao, and Ziming Guo. Formability of ABX_3(X= F, Cl, Br, I) halide perovskites. *Acta Crystallographica Section B: Structural Science*, 64:702–707, 2008.

[91] Mosayeb Naseri, Dennis R Salahub, Shirin Amirian, and Mohammad Abdur Rashid. Computational investigation of Ba_2ZrTiO_6 double perovskite for optoelectronic and thermoelectric applications. *Journal of Solid State Chemistry*, 314:123385, 2022.

[92] Laura Schade, Adam D Wright, Roger D Johnson, Markus Dollmann, Bernard Wenger, Pabitra K Nayak, Dharmalingam Prabhakaran, Laura M Herz, Robin Nicholas, Henry J Snaith, et al. Structural and optical properties of $Cs_2AgBiBr_6$ double perovskite. *ACS Energy Letters*, 4:299–305, 2018.

[93] K Ephraim Babu, A Veeraiah, D Tirupati Swamy, and V Veeraiah. First-principles study of electronic structure and optical properties of cubic perovskite $CsCaF_3$. *Chinese Physics Letters*, 29:117102, 2012.

[94] B Amin, Iftikhar Ahmad, M Maqbool, Souraya Goumri-Said, and R Ahmad. Ab initio study of the bandgap engineering of $Al_{1-x}Ga_xN$ for optoelectronic applications. *Journal of Applied Physics*, 109(2), 2011.

[95] AB Kuzmenko. Kramers–kronig constrained variational analysis of optical spectra. *Review of Scientific Instruments*, 76, 2005.

[96] I Bouziani, M Kibbou, Z Haman, Y Benhouria, Ismail Essaoudi, Abdelmajid Ainane, and Rajeev Ahuja. Electronic and optical properties of ZnO nanosheet doped and codoped with Be and/or Mg for ultraviolet optoelectronic technologies: density functional calculations. *Physica Scripta*, 95:015804, 2019.

[97] Xi Liu, Boming Xie, Chunhui Duan, Zhaojing Wang, Baobing Fan, Kai Zhang, Baojun Lin, Fallon JM Colberts, Wei Ma, René AJ Janssen, et al. A high dielectric constant non-fullerene acceptor for efficient bulk-heterojunction organic solar cells. *Journal of Materials Chemistry A*, 6:395–403, 2018.

[98] Z Haman, M Kibbou, I Bouziani, Y Benhouria, I Essaoudi, Abdelmajid Ainane, and Rajeev Ahuja. Structural, electronic and optical properties of two-dimensional janus transition metal oxides MXO(M=Ti, Hf and Zr; X=S and Se) for photovoltaic and opto-electronic applications. *Physica B: Condensed Matter*, 604:412621, 2021.

[99] Md Roknuzzaman, Kostya Ken Ostrikov, Kimal Chandula Wasalathilake, Cheng Yan, Hongxia Wang, and Tuquabo Tesfamichael. Insight into lead-free organic-inorganic hybrid perovskites for photovoltaics and optoelectronics: A first-principles study. *Organic Electronics*, 59:99–106, 2018.

[100] Jakiul Islam and AKM Akther Hossain. Narrowing band gap and enhanced visible-light absorption of metal-doped non-toxic $CsSnCl_3$ metal halides for potential optoelectronic applications. *RSC Advances*, 10:7817–7827, 2020.

[101] NA Noor, Q Mahmood, M Rashid, Bakhtiar Ul Haq, and A Laref. The pressure-induced mechanical and optoelectronic behavior of cubic perovskite $PbSnO_3$ via ab-initio investigations. *Ceramics International*, 44:13750–13756, 2018.

[102] G Yu, CH Lee, AJ Heeger, and S-W Cheong. Photoconductivity and optical conductivity in lightly doped $Nd_2CuO_{4-\delta}$. *Physica C: Superconductivity*, 203:419–425, 1992.

[103] Eric L Bolda. Theory and simulations of superluminal optical pulses in gain media. *Physical Review A*, 54(4):3514, 1996.

[104] D Mugnai, A Ranfagni, and R Ruggeri. Observation of superluminal behaviors in wave propagation. *Physical Review Letters*, 84:4830, 2000.

[105] Yingzhi Zhou, Jing Wang, Dongxiang Luo, Dehua Hu, Yonggang Min, and Qifan Xue. Recent progress of halide perovskites for thermoelectric application. *Nano Energy*, 94:106949, 2022.

[106] Sile Hu, Zhilin Ren, Aleksandra B Djurisic, and Andrey L Rogach. Metal halide perovskites as emerging thermoelectric materials. *ACS Energy Letters*, 6:3882–3905, 2021.

[107] Andreas Kaltzoglou and Polycarpos Falaras. Recent developments on hybrid perovskite materials for solar energy conversion and environmental protection. *Current Opinion in Chemical Engineering*, 33:100708, 2021.

[108] Thamraa Alshahrani, Ghulam M Mustafa, Tahani H Flemban, Hind Althib, Samah Al-Qaisi, Nessrin A Kattan, and Q Mahmood. Probing of optoelectronic and transport properties of zinc based ZnY_2X_4 (X= S, Se) spinels for renewable energy. *ECS Journal of Solid State Science and Technology*, 9:105001, 2020.

[109] W Tahir, Ghulam M Mustafa, NA Noor, Syed Muhammad Alay-e Abbas, Q Mahmood, and A Laref. Analysis of optoelectronic and trasnport properties of magnesium based $MgSc_2X_4$ (X= S, Se) spinels for solar cell and energy storage device applications. *Ceramics International*, 46:26637–26645, 2020.

[110] E Yu Peresh, VI Sidei, and OV Zubaka. Phase relations in the systems A_2TeI_6-Tl_2TeI_6 (A= K, Rb, Cs) and A_2TeBr_6-A_2TeI_6(A= K, Rb, Cs, Tl (I)). *Inorganic materials*, 41:298–302, 2005.

[111] Oded Rabina, Yu-Ming Lin, and Mildred S Dresselhaus. Anomalously high thermoelectric figure of merit in $Bi_{1-x}Sb_x$ nanowires by carrier pocket alignment. *Applied Physics Letters*, 79:81–83, 2001.

[112] Tsunehiro Takeuchi. Conditions of electronic structure to obtain large dimensionless figure of merit for developing practical thermoelectric materials. *Materials Transactions*, 50:2359–2365, 2009.

[113] Min Hong, Wanyu Lyu, Yuan Wang, Jin Zou, and Zhi-Gang Chen. Establishing the golden range of seebeck coefficient for maximizing thermoelectric performance. *Journal of the American Chemical Society*, 142:2672–2681, 2020.

[114] Rongjian Sa, Yingcong Wei, Wenying Zha, and Diwen Liu. A first-principle study of the structural, mechanical, electronic and optical properties of vacancy-ordered double perovskite Cs_2TeX_6 (X= Cl, Br, I). *Chemical Physics Letters*, 754:137538, 2020.

[115] NA Noor, SM Alay-e Abbas, M Hassan, I Mahmood, ZA Alahmed, and AH Reshak. The under-pressure behaviour of mechanical, electronic and optical properties of calcium titanate and its ground state thermoelectric response. *Philosophical Magazine*, 97:1884–1901, 2017.

[116] Q Mahmood, M Hassan, Tahani H Flemban, Bakhtiar Ul Haq, S AlFaify, Nessrin A Kattan, and A Laref. Optoelectronic and thermoelectric properties of double perovskite Rb_2PtX_6 (X= Cl, Br) for energy harvesting: first-principles investigations. *Journal of Physics and Chemistry of Solids*, 148:109665, 2021.

[117] NA Noor, Muhammad Rashid, SM Alay-e Abbas, Mohsin Raza, Asif Mahmood, Shahid M Ramay, and G Murtaza. Shift of indirect to direct bandgap and thermoelectric response of the cubic $BiScO_3$ via DFT-mBJ studies. *Materials Science in Semiconductor Processing*, 49:40–47, 2016.

[118] Subhash Chandra Lakkad. Temperature dependence of the elastic constants. *Journal of Applied Physics*, 42:4277–4281, 1971.

[119] Quinten A Akkerman, Valerio D'innocenzo, Sara Accornero, Alice Scarpellini, Annamaria Petrozza, Mirko Prato, and Liberato Manna. Tuning the optical properties of cesium lead halide perovskite nanocrystals by anion exchange reactions. *Journal of the American Chemical Society*, 137:10276–10281, 2015.

[120] Yasemin O Ciftci and Meryem Evecen. First principle study of structural, electronic, mechanical, dynamic and optical properties of half-heusler compound LiScSi under pressure. *Phase Transitions*, 91:1206–1222, 2018.

[121] Yiran Ying, Xin Luo, and Haitao Huang. Pressure-induced topological nontrivial phase and tunable optical properties in all-inorganic halide perovskites. *The Journal of Physical Chemistry C*, 122:17718–17725, 2018.

[122] Hillard Bell Huntington. The elastic constants of crystals. In *Solid State Physics*, volume 7, pages 213–351. Elsevier, 1958.

[123] SF Pugh. XCII. relations between the elastic moduli and the plastic properties of polycrystalline pure metals. *The London, Edinburgh, and Dublin Philosophical Magazine and Journal of Science*, 45:823–843, 1954.

[124] Hongzhi Fu, Dehua Li, Feng Peng, Tao Gao, and Xinlu Cheng. Ab initio calculations of elastic constants and thermodynamic properties of NiAl under high pressures. *Computational Materials Science*, 44:774–778, 2008.